Plasma Physics and
Controlled Fusion

PAPER • OPEN ACCESS

Edge fluctuation measurements in EDA H-mode and QCE plasmas in ASDEX Upgrade using the correlation electron cyclotron emission diagnostic

To cite this article: J Schellpfeffer *et al* 2026 *Plasma Phys. Control. Fusion* **68** 015004

IOP Publishing Plasma Phys. Control. Fusion 68 (2026) 015004 https://doi.org/10.1088/1361-6587/ae2d93

Plasma Physics and Controlled Fusion

Check for updates

OPEN ACCESS

RECEIVED
25 June 2025

REVISED
18 November 2025

ACCEPTED FOR PUBLICATION
16 December 2025

PUBLISHED
5 January 2026

PAPER

Edge fluctuation measurements in EDA H-mode and QCE plasmas in ASDEX Upgrade using the correlation electron cyclotron emission diagnostic

J Schellpfeffer[1,*], B Vanovac[1], M Faitsch[2], L Gil[3], L Radovanovic[2,4], N Bonanomi[2], R Bielajew[1], W Burke[1], G D Conway[2], Y Li[1], A Rauschenberger[1], C Yoo[1], A E White[1], the ASDEX Upgrade Team[5] and the EUROfusion Tokamak Exploitation Team[6]

[1] MIT Plasma Science and Fusion Center, Cambridge, MA 02139, United States of America
[2] Max Planck Institute for Plasma Physics, Garching, Germany
[3] Instituto de Plasmas e Fusão Nuclear, Instituto Superior Técnico, Universidade de Lisboa, 1049-001 Lisboa, Portugal
[4] Institute of Applied Physics, TU Wien, Fusion@ÖAW, Vienna, Austria
[5] See Zohm *et al* 2024 (https://doi.org/10.1088/1741-4326/ad249d) for the ASDEX Upgrade Team.
[6] See Joffrin *et al* 2024 (https://doi.org/10.1088/1741-4326/ad2be4) for the EUROfusion Tokamak Exploitation Team.
[*] Author to whom any correspondence should be addressed.

E-mail: jaschell@mit.edu

Keywords: CECE, ELM-free, EDA, QCE, mode, QCM, temperature fluctuations

Abstract

The requirement of a plasma solution without large edge-localized modes (ELMs) for future fusion devices motivates the study of plasmas without Type I ELMs. The enhanced D–α (EDA) and quasi-continuous exhaust (QCE) scenarios are two such Type I ELM free plasmas, but their underlying physics principles are not fully understood. A database of EDA and QCE plasmas from ASDEX Upgrade was compiled and analyzed using the correlation electron cyclotron emission diagnostic in order to study differences between properties of the quasi-coherent mode (QCM) between these two regimes. Investigations into measured spectral properties of the QCM, radiated temperature fluctuations $\delta T_{\mathrm{rad}}/T_{\mathrm{rad}}$, and radial correlation lengths L_{c} showed no differences between the two regimes. Spectral properties using the cross-power spectral density, G_{xy} were similar between regimes, with the values measured to be a central frequency, $f_{\mathrm{QCM}} \approx 20-50$ kHz; spectral width, $\Delta f \approx 5-40$ kHz; $\delta T_{\mathrm{rad}}/T_{\mathrm{rad}} \approx 4-6\%$; and $L_{\mathrm{c}} \approx 1-2$ cm. Investigations into a quantity representing the relative bandwidth $\Delta f/f_{\mathrm{QCM}}$ revealed differences between EDA and QCE plasmas when plotted radially, suggesting some type of interaction between the QCM in QCE plasmas with the surrounding broadband turbulence that is not present in EDA phases. Additionally, investigations into various drive terms for hypothesized instability drivers for the QCM are performed showing no difference in the parameter spaces of collisionality and the ion temperature, electron temperature, or electron pressure scale lengths between each regime indicating that there is no observable difference between the drive behind the QCM in each regime.

1. Introduction

Future fusion power plants require sustainable plasma operation. The presence of large edge-localized modes (ELMs) make the immediate use of high confinement (H-mode) plasmas difficult. ELMs are a consequence of the heightened edge gradients found in H-mode plasmas which themselves are the result of the edge transport barriers that form in H-modes and result in a cyclical ejection of energy and particles out of the plasma [1, 2]. This leads to a continual erosion of plasma facing components and loss of confined particles and energy, and as reactors grow larger in size and fusion power, the threat of ELMs will grow in tandem [3, 4].

A variety of solutions to these large Type I ELMs exist which, to a large part, preserve the good confinement from H-mode without the danger posed by ELMs [5, 6]. Of interest here is the use of *naturally*

Type I ELM-free regimes as opposed to plasmas which are ELM free due to operator intervention such as through resonant magnetic perturbations for example [7]. These naturally Type I ELM-free plasmas display confinement properties on par with standard H-modes but without the presence of large ELMs [8].

The enhanced D_α (EDA) H-mode is one example of a naturally ELM free regime. It was first discovered on Alcator C-Mod and has since been achieved in other experiments including DIII-D and ASDEX upgrade (AUG) among others [9–13]. It is characterized by steady electron densities, radiated power fractions, and the appearance of a ubiquitous edge fluctuation dubbed the quasi-coherent mode (QCM) [14]. The QCM is electromagnetic in nature having been observed through fluctuations in electron temperature, electron density, magnetic field, and electric potential, and it is believed that the QCM is responsible for regulating pedestal transport to the level in which large Type I ELMs are suppressed.

The quasi-continuous exhaust (QCE) regime [15, 16] is a renamed Type II ELM regime [17]. Type II ELMs differ from Type I ELMs in many ways. Most notably, Type II ELMs pose a much lower threat to the materials used in a reactor because they release less energy from the plasma than Type I ELMs. ELM energy loss normalized by the pedestal stored energy is typically <2% for Type II ELMs compared to 2%–15% for Type I ELMs [2].

The QCE regime shares many similarities with the EDA H-mode. In particular, it has similar access conditions [16, 18] and displays a QCM within the same frequency range in AUG plasmas [17, 19]. Due to these similarities, the focus of studying it against the EDA H-mode has gained interest at AUG. Specifically, studies at AUG have compared the properties of the QCM in EDA against those in QCE [20]. Using the thermal helium beam (THB) diagnostic, a difference between spectral widths of the QCM in EDA H-modes and QCE plasmas was observed, with EDA H-modes showing a narrower width than a QCE plasma of similar fueling and power level. Additional differences are found just outside of the separatrix including a more pronounced density shoulder in the scrape off layer (SOL) and increased filamentary activity which leads to broadened heat flux fall-off lengths on the divertor [18, 19]. The subtle differences between the properties or fluctuations of the edge region between two H-modes which display global similarities raises a question on if these two plasmas are of the same regime or distinct from one another. To investigate this question, we look at properties of the QCM.

Conflicting theories on the origin of the QCM remain and it is not certain whether it is driven by some type of resistive or kinetic ballooning mode (RBM or KBM) as suggested in AUG plasmas [20–22], a resistive X-point mode (which is a type of RBM) or drift-Alfven wave instability as suggested by analysis from Alcator C-Mod's EDA H-modes [23, 24], or some type of trapped electron mode as proposed in DIII-D's EDA H-modes [25]. Previous work includes numerous modeling studies which aimed to identify the underlying instability that drives the QCM in the EDA H-mode and QCE regime. From AUG, multiple MHD simulations (including non-ideal and infinite-n ballooning mode) suggest that the QCM in each regime is driven by an RBM type instability near the separatrix [22, 26, 27] matching several experimental observations. Gyrokinetic simulations using GENE have attempted to study the QCM within argon-seeded EDA H-modes in AUG to little success due to technical issues resolving steep gradient effects in the edge [28]. Additionally, experiments which use power and fueling scans have resulted in mixed discharges with transitions between EDA and QCE, further exemplifying the similarities between them. These results, as well as the conflicting theories on the QCM's origin, raise questions about the fundamental physics of each regime, their differences, and their consequences.

This paper complements these previous comparisons by making direct measurements of the spectral properties of the QCM and its associated temperature fluctuations within the pedestal region to the confined edge of the plasma, where the QCM is believed to live. We investigate properties of the QCM in EDA H-modes and QCE scenarios at AUG in order to determine if differences exist in measurable experimental signatures which may explain the previously discussed differences between these two plasmas. The rest of the paper is outlined as follows. Section 2 discusses the experimental set up for this work including an explanation of the correlation electron cyclotron emission (CECE) diagnostic. Section 3 details the analysis carried out using the database of previous AUG discharges. It first describes the creation of the database in section 3.1 followed by an analysis of various measured properties of the QCM in section 3.2. A look into different instability driving terms and their relation to measured fluctuations is done in section 4, and final discussions on the results and a summary of this work are presented in sections 5 and 6, respectively.

2. Experiment details

Properties of the QCM are measured using the CECE diagnostic at AUG [29, 30].

This diagnostic is well suited to the study the QCM and its properties for multiple reasons: 1) it observes fluctuations in the same range of k values that the QCM has been measured in ($k_{\perp}^{\mathrm{CECE}} < 2\,\mathrm{cm}^{-1}$ [31] and $k_{\theta}^{\mathrm{QCM}} \sim 0.6\,\mathrm{cm}^{-1}$ in AUG [11, 20]), 2) CECE measures electron temperature fluctuations which the QCM is associated with [32, 33], and 3) the CECE diagnostic at AUG is capable of measuring in the edge region of the plasma—where the QCM is located—with excellent spatial resolution of 4–5 mm or about 0.01 in ρ_{pol}.

When the discharges included in this paper's database were performed, the system was composed of 24 or 32 (depending on which year the discharge was performed in) channels in a radial configuration. For edge measurements, frequencies of 109–124 GHz are collected with IF filters of 200 MHz bandwidth spaced 250 MHz apart between the center frequencies.

By correlating two neighboring radiometer channels, one is able to preserve turbulent fluctuations while removing the uncorrelated thermal noise from the plasma. Many measurements can be made using CECE, but three main types are focused on; 1) γ_{c}—the coherence between two channels; 2) $\delta T_{\mathrm{e}}/T_{\mathrm{e}}$—the electron temperature fluctuation at a specific location; and 3) L_{c}—the correlation length of a turbulent eddy. Equation (1) shows how γ_{c} is calculated using the time trace of the measured signal from two channels, $x$and y, where $X(f)$ and $Y(f)$ denote the Fourier transform of $x(t)$ and $y(t)$ and $\langle\,\rangle$ denotes an ensemble average,

$$\gamma_{\mathrm{c}}(f) = \frac{G_{xy}(f)}{\sqrt{G_{xx}(f)\,G_{yy}(f)}} \tag{1}$$

$$G_{xy} = \langle X^{*}(f)\,Y(f)\rangle. \tag{2}$$

Because the cross-power, G_{xy}, is a complex quantity, the cross phase between them can be extracted by taking the ratio of the imaginary and real components of G_{xy} [34],

$$\theta_{xy}(f) = \tan^{-1}\frac{\Im\left(G_{xy}(f)\right)}{\Re\left(G_{xy}(f)\right)}. \tag{3}$$

Figure 1 shows the measured γ_{c} of an edge CECE channel pair in a QCE plasma. The frequencies of the two channels used are 109.81 and 109.56 GHz, and each channel is localized to $\rho_{\mathrm{pol}} = 0.987$ and 0.997. Correlating them together averages the locations of the two channels to $\rho_{\mathrm{pol}} = 0.992$. The QCM is seen as a broadband structure with a central frequency around 40 kHz. Fitting the spectra with a Gaussian curve allows one to collect information on the mode's amplitude (A_{QCM}), central frequency (f_{QCM}), and width (Δf) by using the full-width half maximum (FWHM) of the Gaussian. Figure 1 also denotes a sensitivity limit on the calculated γ_{c}. This sensitivity limit represents the level where a calculated signal cannot be statistically distinguished from thermal noise and is calculated as $2\sigma_{\gamma_{\mathrm{c}}}$, where $\sigma_{\gamma_{\mathrm{c}}}$ is the error associated with γ_{c} and $\sigma_{\gamma_{\mathrm{c}}} = (1-|\gamma_{\mathrm{c}}|^2)/\sqrt{2n_d}$, where n_d represents the number of windows used in the ensemble averaging. As a result, higher time-averaged intervals have significantly less statistical error in their results.

There exist many spectral analysis parameters which can be used to study the QCM or similar spectra. Already the cross-power, G_{xy}, and coherence, γ_{c}, have been introduced, but the auto-power, G_{xx}, (which is found using equation (2) for a single channel, x) can be used as well. Frequently within this work, G_{xx} is investigated to identify important frequency bounds for the analysis or identify if the QCM is observed at a single channel's location. Correlation signals like G_{xy} and γ_{c} allow for a more detailed study of the QCM by removing much of the measured thermal noise, and they will be studied in comparison to one another going forward as they contain the same information but present it in different ways due to the normalization used in calculating γ_{c}.

The calculated γ_{c} can be used as in equation (4) to calculate the electron temperature fluctuation, $\delta T_{\mathrm{e}}/T_{\mathrm{e}}$, by integrating over the turbulent feature seen in γ_{c} between two frequency bounds, f_1 and f_2. Here, B_{IF}' represents the IF filter bandwidth of the channel pair and is equal to the square root of the multiple of each channel's bandwidth. γ_{bg} is the background coherence and is used to bias the measured γ_{c} as discussed in [29]. It is calculated by taking the mean of γ_{c} far away from the turbulent feature—in this work the frequency bounds of 200 kHz and 250 kHz are often used.

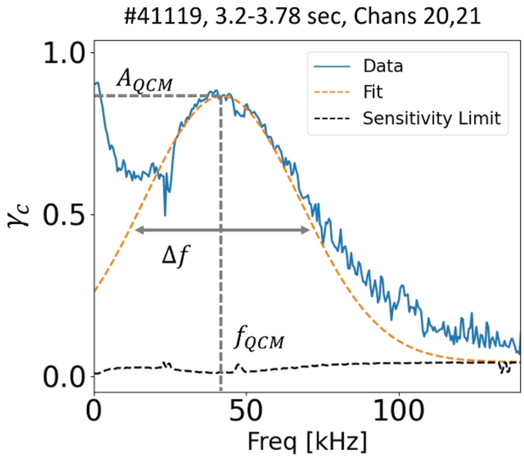

Figure 1. The measured coherence of an edge CECE channel pair ($\rho_{\mathrm{pol}} = 0.99$) in an example QCE plasma. The frequencies of the channels being correlated are 109.81 and 109.56 GHz. The QCM is shown fitted by a Gaussian to collect its properties.

$$\left.\frac{\delta T_{\mathrm{e}}}{T_{\mathrm{e}}}\right|_{xy} = \sqrt{\frac{2}{B'_{\mathrm{IF}}}\int_{f_1}^{f_2}\frac{|\gamma_{\mathrm{c}}(f)-\gamma_{\mathrm{bg}}(f)|}{1-|\gamma_{\mathrm{c}}(f)-\gamma_{\mathrm{bg}}(f)|}\mathrm{d}f} \tag{4}$$

$$B'_{\mathrm{IF}} = \sqrt{B_{\mathrm{IF},x}B_{\mathrm{IF},y}}.$$

Like conventional ECE diagnostics, interpretation of the edge measurements are limited by the optical depth values of the plasma, and one needs a plasma with high enough density and temperature to infer measurements of T_{e} and $\delta T_{\mathrm{e}}/T_{\mathrm{e}}$. In the case of optically thin plasmas, one cannot use a black-body model so measurements of the *radiated temperature* fluctuations $\delta T_{\mathrm{rad}}/T_{\mathrm{rad}}$ rather than $\delta T_{\mathrm{e}}/T_{\mathrm{e}}$ are made. But with careful analysis and plasma design, valuable information can still be obtained from optically thin plasma regions and $\delta T_{\mathrm{rad}}/T_{\mathrm{rad}}$ measurements [35], including a previous use of the CECE diagnostic to study fluctuation levels of the QCM [33]. Because the QCM is found in the plasma edge, the optical depth is often between 1-3 and the plasma is considered optically thin, so in this work, $\delta T_{\mathrm{rad}}/T_{\mathrm{rad}}$ is used when discussing measured temperature fluctuations.

While the CECE diagnostic at AUG is not designed to measure ν_{phase} or k_θ^{QCM}, which other research has measured as a means to understand the instabilities driving the QCM, the profile of $\delta T_{\mathrm{e}}/T_{\mathrm{e}}$ measurements and correlation lengths provides an important characterization of the mode and establishes a solid foundation for future modeling efforts.

3. EDA QCE database analysis

3.1. Database

A database of CECE measurements during QCE and EDA phases from AUG plasmas is assembled to compare various plasma parameters and identify differences in the behavior and possible drives of the QCM in each regime. Discharges are categorized as EDA or QCE based on ELM activity and SOL observations. For example a discharge which shows a clear QCM but also exhibits small ELMs and increased filamentary behavior in the SOL would be QCE. One that is ELM free (including no small ELMs) with a defined QCM is classified as an EDA H-mode.

Table 1 summarizes the range of plasma parameters covered by this database. EDA H-modes and QCE plasmas occur in a very wide parameter space of engineering and plasma parameters [13], and discharges included in the database reflect this. However, limitations to specific plasma parameters are inherent when studying a single region of the plasma over many different discharges. For example, using the CECE diagnostic at AUG requires having a magnetic field strength around 2.5 T for edge measurements and to avoid the negative effects of higher density plasmas, such as refraction or cutoff, plasma currents of ~0.6–0.7 MA are typically used.

When correlating two channels, the presence of any noise peaks they may share is strengthened through the correlation analysis, thus, having a reliable method to filter out these noise peaks is imperative to a database study such as this. Following the procedure used in [36], a moving average, threshold-based filter was used to remove these narrow electronics noise peaks from G_{xx}, G_{xy}, and γ_{c} spectra.

Table 1. Values of common plasma parameters for discharges included in the database. Edge quantities were taken at $\rho_{pol} = 0.95$.

Parameter	Edge n_e [10^{19}m^{-3}]	Edge T_e [eV]	I_p [MA]	ν^*_{ped} [−]	q_{95} [−]	P_{input} [MW]	β_{pol} [−]	B_t [T]
D, EDA	4.1–6.6	210–380	0.6–0.7	3.1–7.9	5.6–7.3	1.2–3.4	0.7–1.4	2.48–2.53
D, QCE	4.1–5.6	290–480	0.6–0.6	2.7–7.4	7.5–7.9	4.2–6.9	1.2–1.9	2.48–2.50
He, EDA	4.5–5.8	270–360	0.7–0.7	3.7–6.4	5.5–5.6	2.5–3.1	0.9–1.0	2.48–2.48
Full Database	4.1–6.6	210–480	0.6–0.7	2.7–7.9	5.5–7.9	1.2–6.9	0.7–1.9	2.48–2.53

Table 1 includes calculated pedestal collisionality values, ν^*_{ped}. This is calculated at $\rho_{pol} = 0.95$ using,

$$\nu^* = 6.9 \times 10^{-18} \frac{R q_{95} Z_{eff} \ln\Lambda n_e}{\epsilon^{3/2} T_e^2}, \tag{5}$$

$$\ln\Lambda = 31.3 - \ln\left(\sqrt{n_e}/T_e\right).$$

Here, n_e is the electron density in units of m^{-3}, T_e is the electron temperature in units of eV, R represents the major radius of the plasma in meters, q_{95} the safety factor at $\rho_{pol} = 0.95$, Z_{eff} is the effective ion charge of the plasma, and ϵ is the inverse aspect ratio [37]. $\ln\Lambda$ is the quantum Coulomb logarithm [38].

When values of n_e and T_e are used in the analysis, their values are obtained from modified hyperbolic tangent fits to Thomson Scattering and ECE measurements [39]. Z_{eff} is calculated through the integrated data analysis framework using measured Bremsstrahlung radiation [40].

Multiple time phases from a single discharge may be included in the database if plasma parameters show significant change (for example during heating or fueling scans). The majority of phases are performed in a D plasma, but a few select discharges have been performed in He allowing for the inclusion of non-D plasmas. These He plasmas had phases in EDA H-mode and including them allows for a preliminary study of main ion differences that may exist and affect the QCM observed in EDA H-mode. In total, 36 phases are included in the database with a breakdown of 19 EDA H-modes in D, 8 QCE plasmas in D, and 9 EDA H-modes in He. A full list of included discharges and time periods is included in the appendix.

3.2. Database analysis

Phases included in the database can be analyzed using the methods outlined in section 2. Properties obtained from fits to the QCM spectra are looked at first, including differences between the type of spectra measured (i.e. γ_c vs G_{xy}). Radial profiles for the quantities $\delta T_{rad}/T_{rad}$, a calculated quantity which uses $\delta T_{rad}/T_{rad}$ called the displacement, ξ, and L_c are plotted for each discharge and observed trends are noted. Finally, behaviors in the cross phase between CECE channels (equation (3)) of different plasma types are investigated and compared to other standard regimes at AUG such as I-modes and Type I ELMy H-modes.

3.2.1. QCM spectral properties

Many spectral properties of the QCM can be extracted by using Gaussian fits. For example, figure 1 shows a coherence spectra fitted with a Gaussian curve, but the same can be done for an auto-power or cross-power spectra due to the strong visibility of the QCM in each signal as shown in figure 2. Properties of the QCM are measured using the fitted Gaussian such as the mode's amplitude (A_{QCM}), frequency width (Δf) by using the FWHM definition, and central frequency (f_{QCM}). Comparing the widths obtained using fits from γ_c and G_{xy} shows that the QCM width is larger when quantified by γ_c as compared to G_{xy}. This is observed in all phases of the database irrespective of plasma type or main-ion. Values for the width obtained using G_{xy} range between 5 and 40 kHz whereas values obtained using γ_c range between 20 and 70 kHz. Fits produced using the auto-power give widths in the same range as those from the cross-power. The differences in the measured widths of G_{xy} and γ_c are not the result of new information which G_{xy} does not include, but is in fact due to the normalization that is used when calculating γ_c. Because of this normalization, γ_c is much more sensitive to resolving low level turbulence which broadens the Gaussian like spectra. As a result, the *fits* to γ_c include additional information that is not captured in the fits to G_{xx} or G_{xy}. Conversely, the central frequencies obtained using each spectra type for a given phase in the database are approximately constant radially as shown in figure 3. Here, f_{QCM} from a single EDA discharge (#40821 4.68–6.05 s) is plotted against the location of the channel or channel pair used to calculate the respective spectra. There is an offset between the locations of the

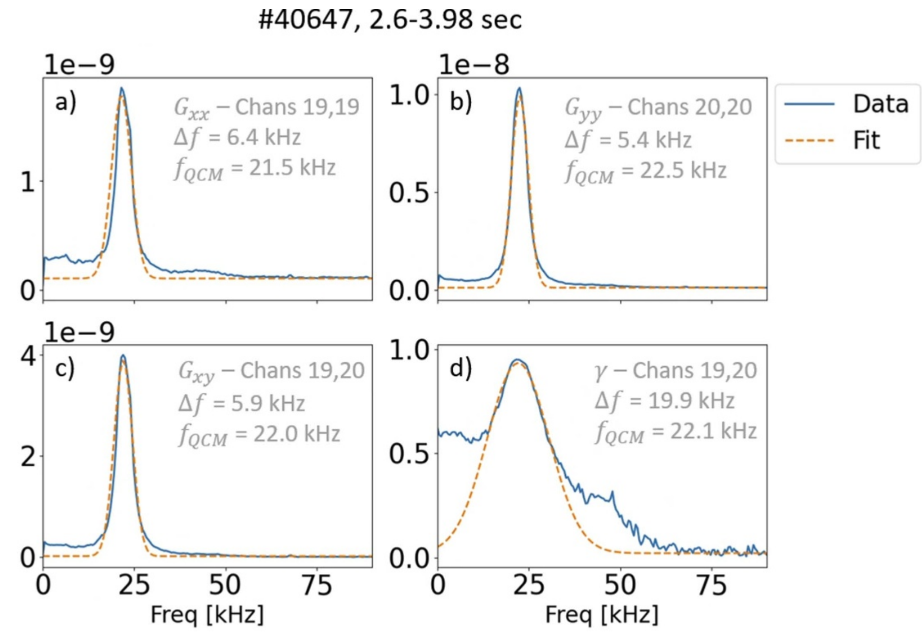

Figure 2. Plots of measured spectra of the QCM in an EDA discharge showing in (a) auto-power of the first channel, G_{xx}, (b) auto-power of the second channel, G_{yy}, (c) cross-power, G_{xy}, and (d) coherence, γ_c. As shown, the mode is visible within all spectra with minimal changes to the QCM central frequency between each, but the width of γ_c is significantly broadened when compared to G_{xx}, G_{yy}, and G_{xy}. All subplots show measured data in blue and the corresponding Gaussian fit in orange.

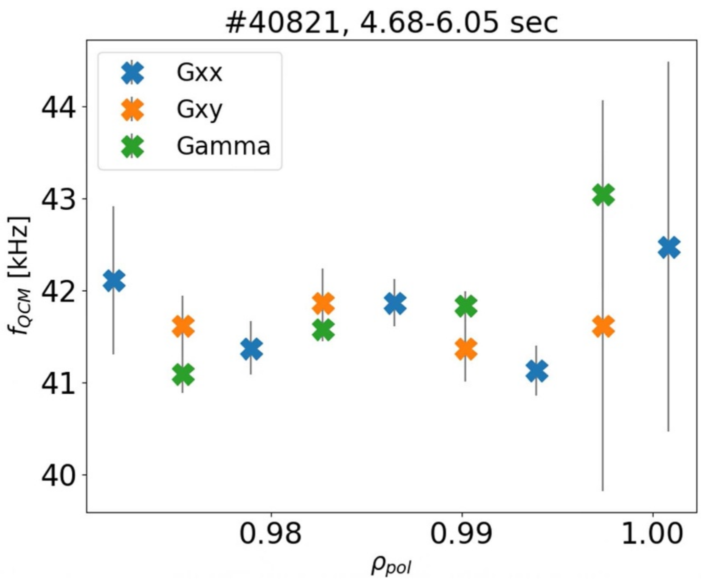

Figure 3. Fitted values of the central frequency for a single phase of an EDA discharge in the database. Shown are values for G_{xx} (blue), G_{xy} (orange), and γ_c (green). All values are in agreement within 1 kHz showing that the QCM frequency is radially constant.

blue (G_{xx}) and orange or green (G_{xy} or γ_c) marks since the cross-power and coherence spectra take the average of each channel's location used in the correlation.

Combining spectral properties allows for an exploration into the behavior of the QCM in new ways. For example, a quantity can be calculated by dividing the spectrum's width by its central frequency, $\Delta f/f_{\mathrm{QCM}}$. [20] calls this quantity the *coherency*, but to avoid confusion with the coherence γ_c, it is referred to as a quantity of *relative bandwidth* in this work.

This is first done using data from fits to G_{xy}, where this value is plotted against the radial distribution of channel positions in figure 4(a). Figure 4(b) and c shows the components of this ratio, with figure 4(b) showing Δf_{QCM} and figure 4(c) showing f_{QCM}, and dashed lines indicate channels from the same discharge and time interval. All phases are included with the colors, red and blue, distinguishing

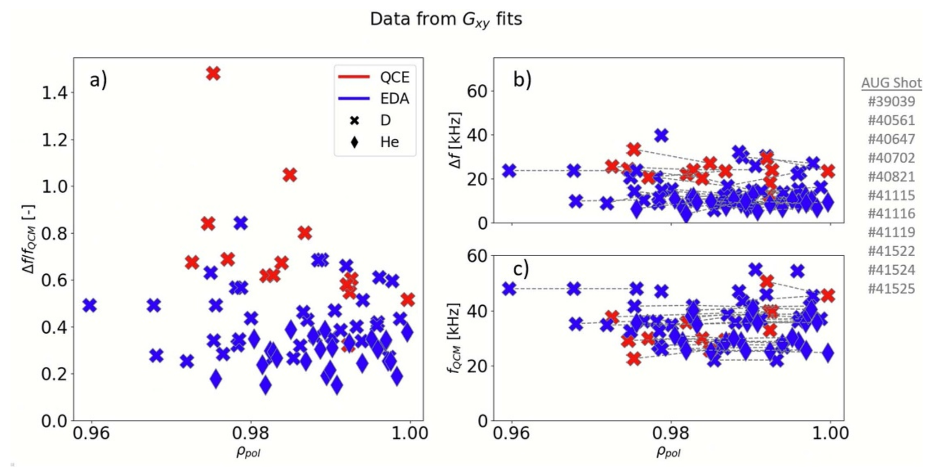

Figure 4. The relative bandwidth ($\Delta f/f_{\mathrm{QCM}}$) is shown in (a) calculated using fits to G_{xy}. As shown to the right in (b) and (c) respectively, Δf and f_{QCM} are essentially constant radially and $\Delta f/f_{\mathrm{QCM}}$ in both EDA and QCE plasmas show strong overlap in all ρ_{pol} values. D and He EDA discharges display similar behavior between each other. Dashed lines are used in (b) and (c) to indicate measurements from the same discharge/time interval in the database.

QCE and EDA plasmas and shapes, x's and diamonds, distinguishing main ions D and He respectively. This will be the labeling scheme for all scatter plots going forward. Additionally, all plots that are created from multiple discharges in the database list those discharges to the right of the figure throughout the paper.

Investigating the behavior of figure 4(a) reveals a large amount of scatter for EDA discharges. This is true for both D and He plasmas within the database. However, there is a slight subtle trend for QCE discharges that shows a decreasing trend between $\Delta f/f_{\mathrm{QCM}}$ and an increasing ρ_{pol}. However, when applying the same analysis to data obtained from fits to γ_{c}, the trends become much more visible as seen in figure 5(a). Though there is still a large amount of scatter within EDA plasmas (again, both D and He), there appears to be a small positive trend. For QCE discharges, the subtle negative trend observed with data from G_{xy} increases in strength. A transition point appears around $\rho_{\mathrm{pol}} \sim 0.98$ where the behavior of QCE and EDA discharges diverge. For $\rho_{\mathrm{pol}} < 0.98$, the data is separated, but for $\rho_{\mathrm{pol}} > 0.98$ they occupy the same parameter space. This is most clear in figure 5 as compared to figure 4. However, the fact that a difference in trends is more visible using γ_{c} but not when using G_{xy} is not because each quantity contains different physics about the data. In fact, neither figure presents a more accurate depiction; they merely show the same data differently. γ_{c} is a normalized version of G_{xy}, and this normalization allows it greater sensitivity to pick out and highlight features from low level turbulence that cannot be seen in G_{xy} alone. As such, figure 5 presents subtle trends that figure 4 is unable to show. This, along with the fact that the frequency remains constant radially for a given discharge and time interval (shown in figure 3), implies that the increase in γ_{c}'s width is driven by an increase of the broadband turbulence surrounding the QCM.

3.2.2. Temperature fluctuations

Figure 6 shows the radial distribution of measured radiated temperature fluctuations for phases within the database. Consistent trends are observed between all discharges; a nearly constant value is observed in the outer core region to the pedestal top, $\rho_{\mathrm{pol}} \approx 0.90 - 0.97$, with values increasing within the steep gradient region and peaking at 5%–6% just before the separatrix, $\rho_{\mathrm{pol}} \approx 0.99$. Values of $\delta T_{\mathrm{rad}}/T_{\mathrm{rad}}$ between D EDA and He EDA discharges are quite similar in fluctuation levels across the edge of the plasma.

It is worth noting that measurements at the edge are within an optically thin region where the measured intensity cannot be treated like a black-body emission. The location between an optically thick and thin region varies across the database, but due to the high densities of these plasmas, it is generally around $\rho_{\mathrm{pol}} \approx 0.97 - 0.98$. For measurements past this location, we measure fluctuations in the radiated temperature, $\delta T_{\mathrm{rad}}/T_{\mathrm{rad}}$, not necessarily fluctuations in the electron temperature.

A forward model of the measured intensity which takes into account variations in the optical depth, τ, due to changes in T_{e} and n_{e} can set limits on the proportion of measured intensity that is contributed by temperature or density fluctuations. However, the phase between the density and temperature fluctuations is needed to accurately account for this effect. A forward model has been applied in the past

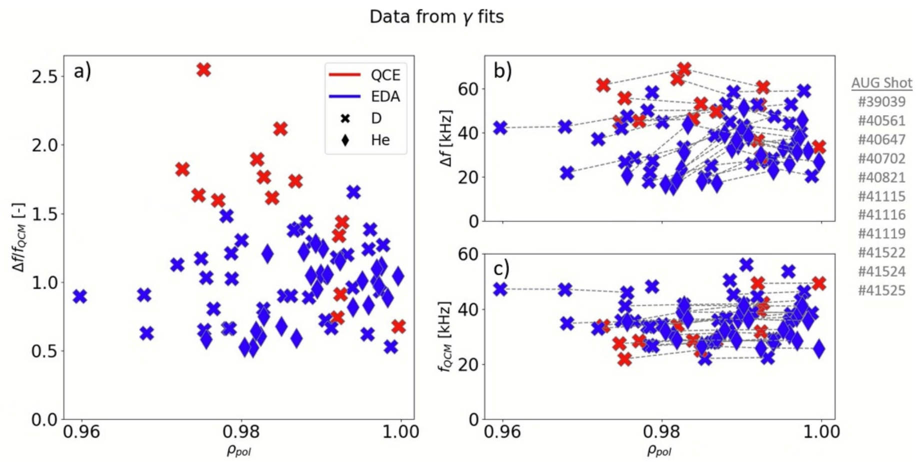

Figure 5. The relative bandwidth ($\Delta f/f_{\mathrm{QCM}}$) is shown in (a) calculated using fits to γ_c. As shown to the right in, (b) Δf changes radially, but (c) f_{QCM} is constant resulting in differing trends between EDA and QCE plasmas. Dashed lines are used in (b) and (c) to indicate measurements from the same discharge/time interval in the database.

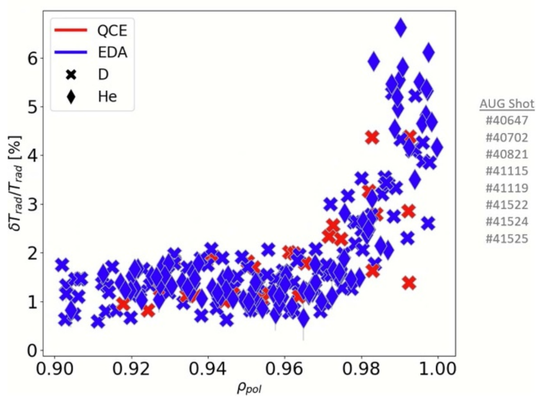

Figure 6. A scatter plot of measured radiation temperature fluctuations for all discharges included in the database. Consistent trends are observed between all phases with a peak observed in the edge of the confined region.

[41, 42], and in the future, we plan to use direct measurements of this phase difference from a correlation reflectometer-radiometer diagnostic [43] with this type of forward model to better understand the impact that density fluctuations have on the radiation temperature in such situations. But for this work, the measurement of $\delta T_{\mathrm{rad}}/T_{\mathrm{rad}}$ is still used for studies of the QCM in the edge region.

Measured temperature fluctuations are compared against the central frequency of the QCM to reveal differences in the trends between plasma types in figure 7. Whereas there is a slight, positive correlation for QCE plasmas, EDA H-modes show a slight negative correlation, albeit with greater scatter. However, interpretation of any trends observed between these two parameters presents a significant challenge. Not only could there be hidden variables that change throughout this database which may affect each parameter, but the range of scatter which exists provides a strong possibility for false trends to present themselves. Even the less scattered QCE points occupy the same parameter space as EDA, so it could be that because the database contains less QCE phases than EDA, the QCE parameter space cannot be fully populated and the included subset presents a false narrative.

3.2.3. Displacement

It is common in MHD theory to use a parameter called the displacement, ξ, for mode localization, with the mode being localized to where the displacement it creates is greatest. Temperature fluctuations are used in tearing mode theory to calculate ξ as shown in equation (6) [44],

$$\xi = \left(\frac{\delta T_{\mathrm{e}}}{T_{\mathrm{e}}} * T_{\mathrm{e}}\right) / \nabla T_{\mathrm{e}}. \tag{6}$$

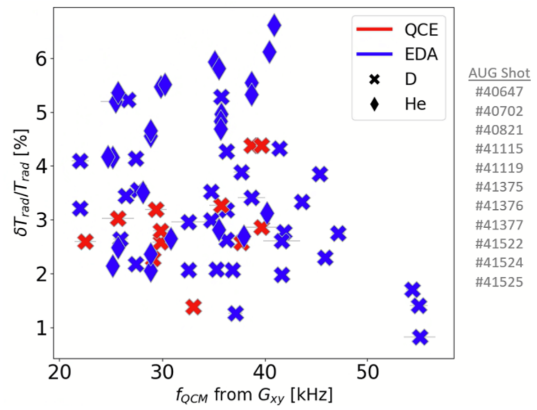

Figure 7. Opposing trends are observed between EDA and QCE plasmas when plotting $\delta T_{\mathrm{rad}}/T_{\mathrm{rad}}$ against f_{QCM}. A trend of opposite sign is observed for QCE phases compared with EDA phases, but due to the range of scatter within EDA phases, it is not clear if this is a false trend due to less QCE discharges within the database.

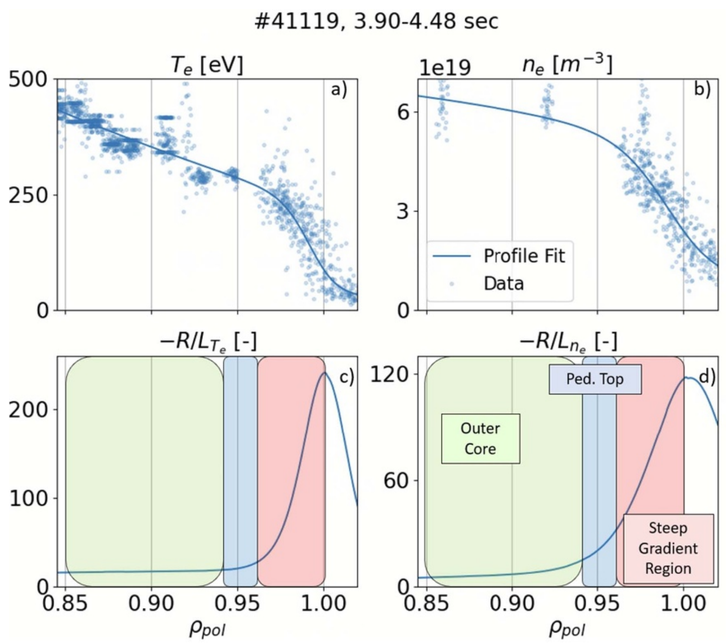

Figure 8. Profiles fit to experimental data for (a) T_{e} and (b) n_{e}. The gradient scale lengths, $-R/L_{T_{\mathrm{e}}}$ and $-R/L_{n_{\mathrm{e}}}$ are shown in (c) and (d), respectively ($L_X = X/\nabla X$ for $X = T_{\mathrm{e}}$ or n_{e} and R being the major radius). Shown in (c) and (d) are shaded regions indicating different regions of the plasma used in the analysis with green shading for the outer core, blue shading for the pedestal top, and red shading for the steep gradient region.

Normalizing by the electron temperature gradient converts the absolute temperature fluctuation, $\delta T_{\mathrm{e}}/T_{\mathrm{e}} * T_{\mathrm{e}}$, from units of eV to a length scale. This calculation can be performed for each phase in the database for each channel of the diagnostic to create a similar radial profile as figure 6. $\delta T_{\mathrm{e}}/T_{\mathrm{e}}$ is directly measured by the CECE diagnostic, and T_{e} and ∇T_{e} are evaluated at the same radial location as $\delta T_{\mathrm{e}}/T_{\mathrm{e}}$. Values of the electron temperature profile and its gradients are taken from modified hyperbolic tangent fits [39] to data collected by core and edge Thomson scattering systems and ECE systems. As an example, figure 8 shows the profile fits for T_{e} and n_{e} for a single phase of an EDA discharge. The raw data for each quantity is shown as slightly transparent points and the produced fit as a solid line. Electron pressure profiles are calculated using the profiles of temperature and density, and gradients for all three quantities are numerically taken from the resulting fits.

Figure 9 shows values of ξ against ρ_{pol} for discharges within the database. Generally, QCE and EDA points are indistinguishable from one another and occupy similar values across the measured radial range. Of particular interest are the points of ξ located at the edge, $\rho_{\mathrm{pol}} \approx 0.97-0.98$, and reach values of $\xi \approx 10$ mm. Unlike in figure 6, values are peaked at a more inward location in the plasma and the

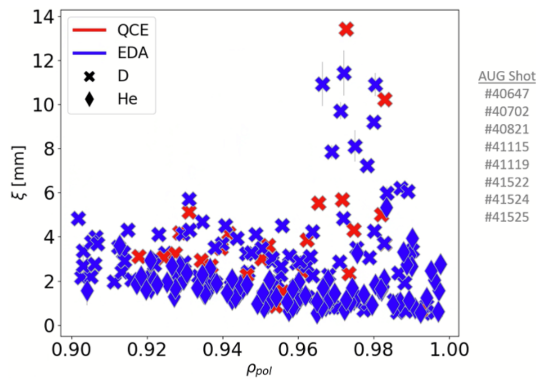

Figure 9. Values of ξ are plotted for discharges in the dataset. Most discharges peak at ρ_{pol} values of $\approx 0.97-0.98$ and there is a general decrease as ρ_{pol} increases towards the separatrix.

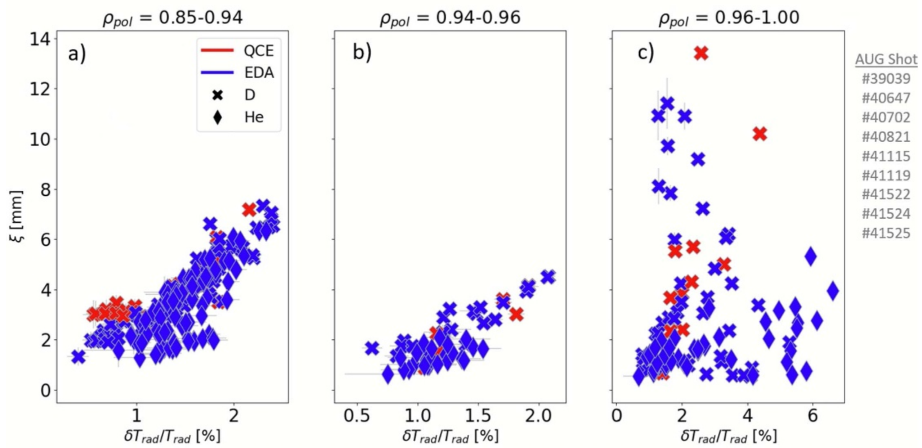

Figure 10. For all discharges in the dataset, calculated values of ξ are plotted against the measured values of $\delta T_{\mathrm{rad}}/T_{\mathrm{rad}}$ for three different radial regions corresponding to the outer core up to the pedestal top, the pedestal top region, and the steep gradient region. For all regions, except the steep gradient region, a linear trend is seen between ξ and $\delta T_{\mathrm{rad}}/T_{\mathrm{rad}}$.

range of peaked locations is broader. The trends presented in figure 9 are generally more scattered than those in figure 6.

To better investigate the relation between ξ, $\delta T_{\mathrm{e}}/T_{\mathrm{e}}$, and the resulting peak observed in figure 9, ξ and $\delta T_{\mathrm{e}}/T_{\mathrm{e}}$ are plotted against one another in figure 10. $\delta T_{\mathrm{rad}}/T_{\mathrm{rad}}$ is used in place of $\delta T_{\mathrm{e}}/T_{\mathrm{e}}$ here because of the measurements taking place in optically thin regions close to the separatrix, as discussed in section 2. The data is split into three radial regions within figure 10; $\rho_{\mathrm{pol}} = 0.85-0.94$ corresponding to the outer core region up to the pedestal top, $\rho_{\mathrm{pol}} = 0.94-0.96$ for the pedestal top region, and $\rho_{\mathrm{pol}} = 0.96-1.00$ for the step gradient region. From this, one can notice two things, (1) the highest values of ξ occur at moderate values of $\delta T_{\mathrm{rad}}/T_{\mathrm{rad}}, \approx 2.5\%$ and (2) ξ and $\delta T_{\mathrm{rad}}/T_{\mathrm{rad}}$ have a near linear relationship for all locations outside of the steep gradient region. Even within the steep gradient region, there is a near linear trend until $\delta T_{\mathrm{rad}}/T_{\mathrm{rad}}$ values of $\sim 2\%$ at which point ξ values diverge. From equation (6), it can be seen that ξ is maximized for higher values of $\delta T_{\mathrm{rad}}/T_{\mathrm{rad}}$ or lower values of ∇T_{e}. The strongest values of $\delta T_{\mathrm{rad}}/T_{\mathrm{rad}}$ are measured in the edge where ∇T_{e} is also strong, so the largest values of ξ occur where moderate fluctuations are measured but ∇T_{e} is weaker and cannot fully minimize the calculation.

Figure 11, shows the mismatch in peaked locations between ξ and ∇T_{e} in an alternative way by splitting up different phases of the database: D EDA plasmas, D QCE plasmas, and He EDA plasmas. For D EDA and QCE plasmas, there is a visible difference in peaked locations for $\delta T_{\mathrm{rad}}/T_{\mathrm{rad}}$ and ξ, but for He, EDA plasmas, $\delta T_{\mathrm{rad}}/T_{\mathrm{rad}}$ is co-located in the ∇T_{e} well, minimizing the majority of peaks that would appear in ξ. A small peak is still present in ξ for He, EDA, but it is much less significant than D, EDA or QCE. The reason for this is the same as why peaks in ξ are observed in D EDA and QCE around ρ_{pol} of 0.97; there is still a moderate value of $\delta T_{\mathrm{rad}}/T_{\mathrm{rad}}$ when ∇T_{e} reaches values closer to zero. However, the peak in He, EDA is not as strong as in either case in D because these two regions share greater overlap in He unlike in D. For D EDA plasmas, the peaked region in ξ appears to be well separated from the

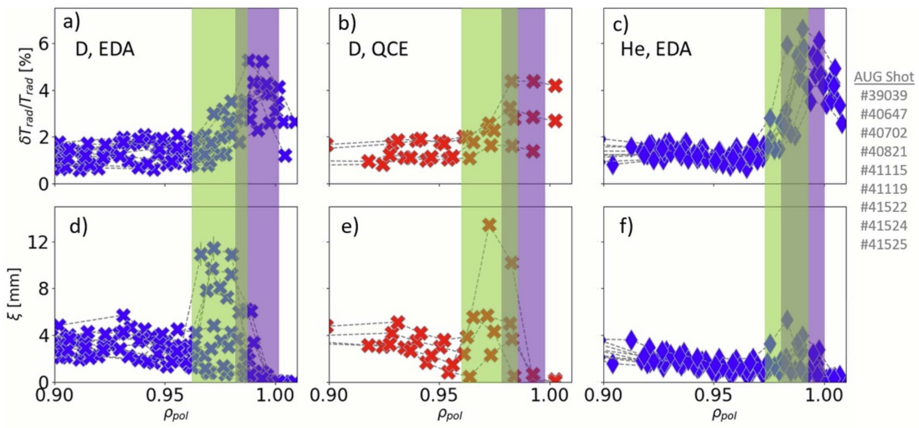

Figure 11. Radial plots of $\delta T_{\mathrm{rad}}/T_{\mathrm{rad}}$ plotted on top of radial plots of ξ for each phase of data in the database. Peaked regions of $\delta T_{\mathrm{rad}}/T_{\mathrm{rad}}$ are highlighted in purple and peaked regions of ξ are highlighted in green.

peaked region in $\delta T_{\mathrm{rad}}/T_{\mathrm{rad}}$, but there is an overlap in peaked regions of ξ and $\delta T_{\mathrm{rad}}/T_{\mathrm{rad}}$ for D QCE plasmas and especially He EDA plasmas.

The conflicting peaked regions between $\delta T_{\mathrm{rad}}/T_{\mathrm{rad}}$ and ξ raise some concerns about where the mode should be localized. On the one hand, the profile of $\delta T_{\mathrm{rad}}/T_{\mathrm{rad}}$ shows a peak at a location very close to the separatrix which closely matches the area of strongest E_{r} and previous localizations of the QCM based on other fluctuating quantities such as $\delta n_{\mathrm{e}}/n_{\mathrm{e}}$. However, radiometers are sensitive to strong temperature gradients in which the gradient at the origin of the radiation has a significant impact on its trajectory in cases where 2D effects are significant such as refraction [33], and, in this work, the maximum fluctuation is strongest where ∇T_{e} is strongest. Normalizing by ∇T_{e} attempts to correct for this inherent sensitivity to reveal the full extent of a measured perturbation. In this case, signatures of the QCM can be observed up towards the pedestal top, not just close to the separatrix. Yet, because ξ only takes into account temperature fluctuations, it inherently discounts fluctuations in other parameters that the QCM is known to induce. As such, it cannot capture the full picture. The result is that $\delta T_{\mathrm{rad}}/T_{\mathrm{rad}}$ better captures the localization of the QCM, and it is agreement with the well of the radial electric field (where the QCM has been localized to in previous works) supports this.

3.2.4. Correlation length

The radial correlation length, L_{c}, of the QCM can be measured using the CECE diagnostic by correlating sequential channels to a single reference channel. More specifically, the correlation coefficient at zero time delay ($C_{xy}(\tau=0)$) is calculated from the cross-correlation function of the time histories of two channels $x(t)$ and $y(t)$ as shown in equation (7) [34]. Unlike when calculating γ_{c} or $\delta T_{\mathrm{e}}/T_{\mathrm{e}}$ where each neighboring channel pair is correlated, here, a single *reference* channel, x, is correlated with 4 or 5 of its neighboring channels, y, and a function of $C_{xy}(\tau)$ is calculated for each channel pair [45]. Next, an envelope (E) is fit to $C_{xy}(\tau)$ using the Hilbert transformation of C_{xy} using equation (8) [46]. By taking the value of the envelope at zero time delay ($E(\tau=0,\Delta r)$) and plotting it against the distance between each channel pair (Δr), a Gaussian curve can be fit (using the amplitude (A), width (w), and linear offset (b) as free parameters), and the $1/e$ falloff length is found and taken to be the measured correlation length L_{c} of a turbulent feature. The function that is used in this fit is shown in equation (9). Repeating this process for multiple reference channels gives a radial distribution of L_{c},

$$C_{xy}(\tau) = \frac{\langle x(t)\,y(t+\tau)\rangle}{\sqrt{\langle x(t)^2\rangle\langle y(t)^2\rangle}} \tag{7}$$

$$E = \sqrt{C_{xy}^2 + H\left(C_{xy}^2\right)} \tag{8}$$

$$E(\tau=0,\Delta r) = A\exp-(\Delta r/w)^2 + b. \tag{9}$$

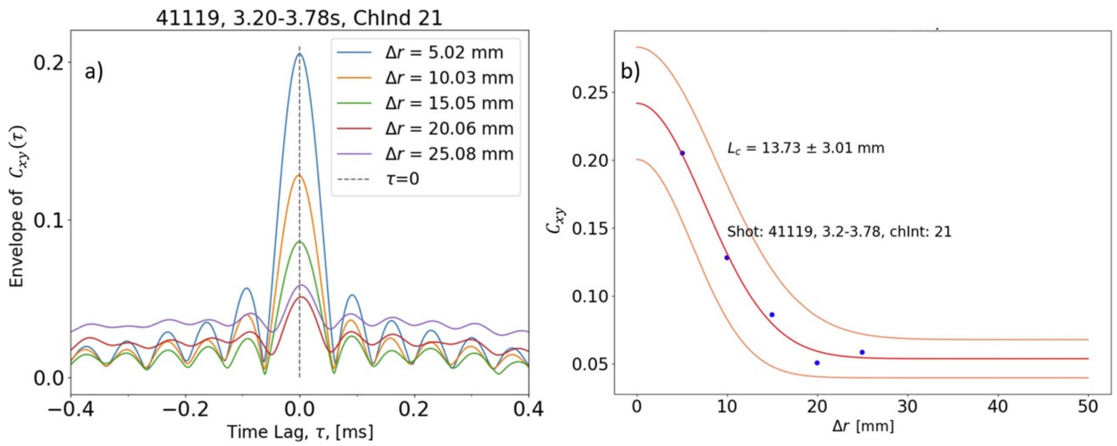

Figure 12. The process of calculating L_c for a single reference channel is shown. (a) The correlation between each channel pair and the envelope fit to each correlation function. (b) The resulting fit using equation (9).

Figure 12 gives an example of this process using a QCE plasma from discharge #41119, 3.2–3.78 s and channel 21 in the edge as the reference.

However, an additional, preliminary step in the calculation of L_c is performed to eliminate contributions from thermal noise and highlight the mode of interest (in this case the QCM). The two signals, $x(t)$and $y(t)$ are Fourier transformed and a bandpass filter using the frequency bounds of the QCM is applied. The frequency bounds are found for each unique discharge and time interval studied by investigating the auto-power spectral density of each channel, G_{xx}. The signals are transformed back to time traces and the analysis continues as explained in the preceding paragraph. This is possible to do because the QCM is a strong enough mode that it is visible on a single radiometer channel without needing to correlate neighboring channel pairs, so frequency bounds can be selected using G_{xx}. This filtering method is shown in figure 13. As well, when fitting the values of $C_{xy}(\tau = 0)$ to find L_c, the self correlation of C_{xx} is not included as $C_{xx}(\tau = 0)$ is equal to 1 by definition.

Measurements of L_c for the QCM are shown for various radial positions in figure 14. Fewer channels are included than in previous scatter plots due to the requirement of having a well defined QCM observed in a single channel before any correlation techniques are applied. This is done to avoid correlating two channels which do not capture the QCM and producing a radial correlation length of some other turbulent feature. Thus, only channels around the pedestal top and in the steep gradient region had sufficiently good data which could be used to calculate L_c.

Even so, a clear trend can be observed—higher values of L_c occur towards the pedestal top, ≈ 2 cm, and at regions within the steep gradient region, L_c decreases to a value of ≈ 1 cm. The decrease in L_c indicates a smaller scale length of measured turbulence, indicative of strong shear, such as from a deepened radial electric field (E_r) well and the resulting, higher $E \times B$ velocities.

The region of minimum L_c is the same region where the strongest values of $\delta T_{rad}/T_{rad}$ are observed. If the QCM is localized to this location, it would be within the E_r well, which coincides with measurements from Alcator C-Mod EDA H-modes [47].

3.2.5. Phase differences

Previous sections have looked at common QCM-related parameters that one can measure using the CECE diagnostic, and, generally, no distinction between the EDA and QCE regimes are observed. We now investigate the phase of the mode with respect to channel location. Introduced in section 2, the phase difference, θ_{xy} between two channels $x$and y comes about from the calculation of the complex cross-correlation G_{xy}, and in many uses of CECE, θ_{xy} is primarily used to identify a real turbulent signal when a steady θ_{xy} is observed rather than randomly varying values [48]. Figure 15 shows this principle by plotting γ_c and θ_{xy} from an EDA plasma. Additionally, if there exists a poloidal separation between two CECE channels, the slope of θ in frequency can be used to estimate the poloidal velocity of the turbulent mode as it moves across the two channels [35].

Here, θ_{xy} is used to investigate the fundamental physics driving each regime to try and identify differences between each. To do so, the phase difference is calculated for all edge channels which show the

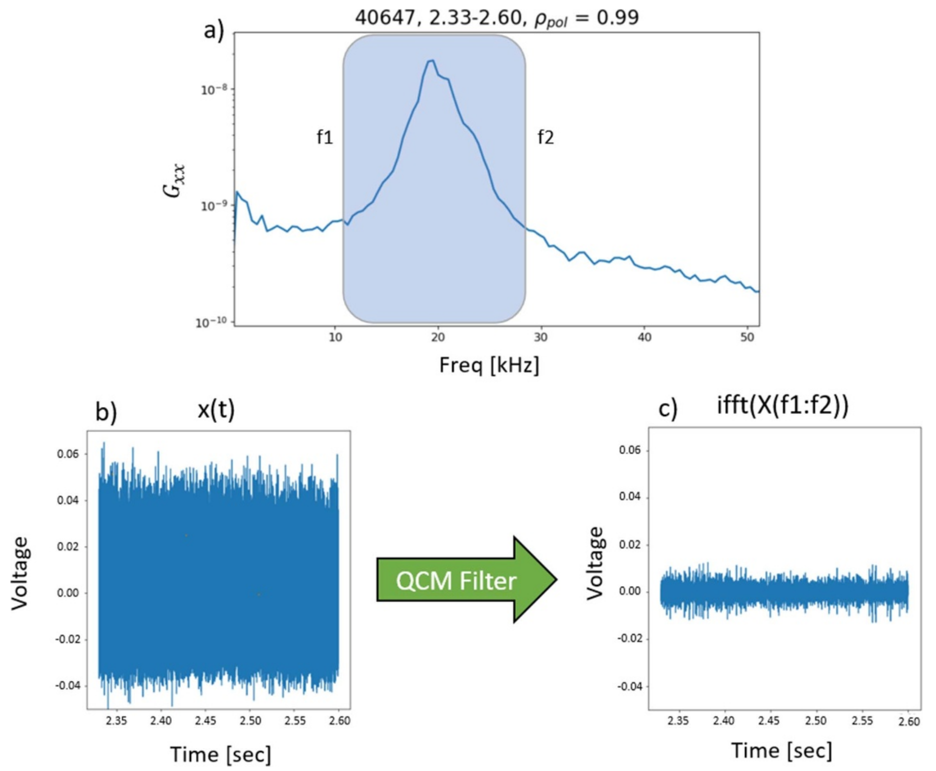

Figure 13. A bandpass filter is applied to the auto-power spectra of a channel to highlight the QCM before calculating L_c. (a) The auto-power is used to identify the frequency bounds of the QCM for the bandpass filter (f1 and f2), (b) the pre-filtered time history of channel x, and (c) the post-filtered time history of channel x with only the QCM signal present.

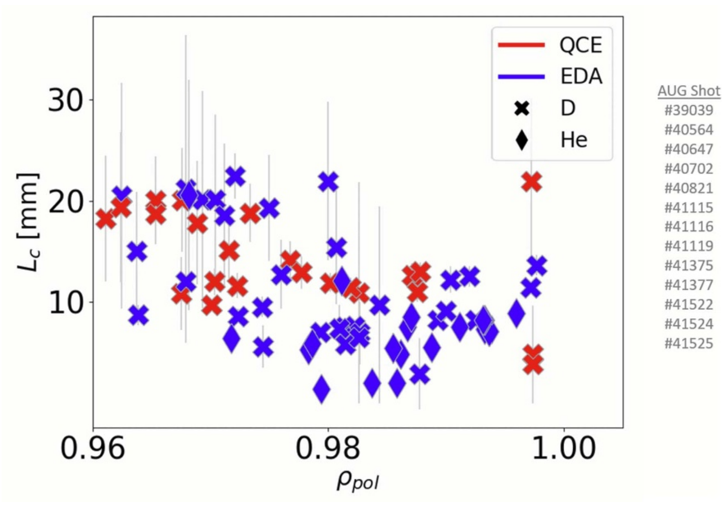

Figure 14. Measured correlation lengths of discharges in the database. A decrease in the value L_c occurs in the steepest gradient region.

QCM in their auto-power signal, $G_{xx}(f)$. Each of these channels are cross-correlated with all other channels to get the cross-power spectra and associated phase difference, $G_{xy}(f)$and $\theta_{xy}(f)$ for $y = [1,2,3,4....]$. The phase difference is then averaged over the QCM's frequency bounds (as determined using the auto-power spectra), and this value is plotted at the radial location of channel, y. This process gives the evolution of the phase difference in space, up to and across the QCM. Figure 16 shows this for a single EDA discharge, #40821 between 4.68 and 6.05 s, using a reference channel located at $\rho_{\mathrm{pol}} = 0.99$ which is where the QCM amplitude is strongest for this time phase. A constant phase difference is observed between channels in the outer core region with those capturing the QCM. This trend holds up to the pedestal top where a sharp increase (decrease) in the phase difference (magnitude) occurs. Those channels measuring the QCM show a small positive phase difference with respect to the reference channel.

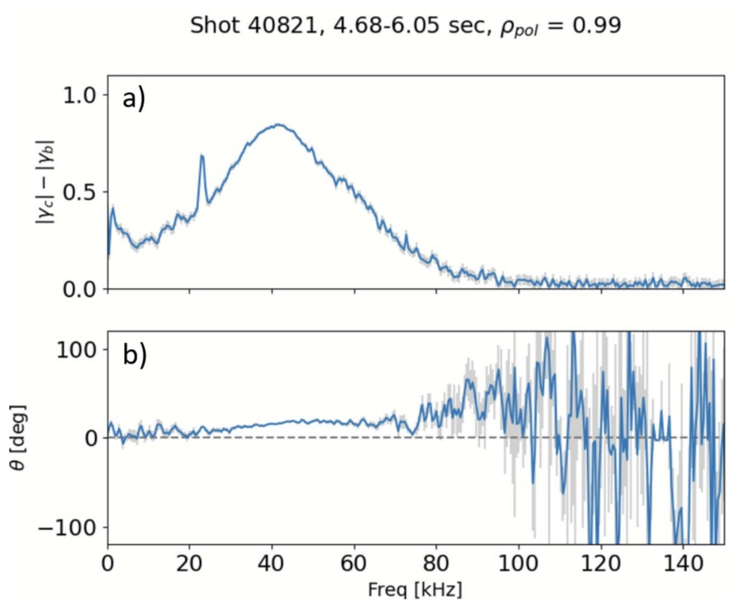

Figure 15. The (a) coherence spectra and (b) phase difference are plotted over the same frequency range. At the same frequencies that the coherence shows the QCM, the phase difference rises at a steady rate. Outside of this frequency range, the phase difference is random.

These trends are consistently observed for all EDA phases within the database. Additionally, the same behaviors are seen consistently in QCE phases as well.

For comparison, this analysis was repeated using other plasma regimes including an L-mode (#40821 1.0–1.8 s), standard H-mode (#40254 2.1–2.6 s), and I-mode (#38493 5.0–5.9 s). The results for each of these discharges are shown in figure 17 along with a representative discharge for EDA (#40647 4.33–6.0 s) and QCE (#41119 3.2–3.78 s) phases. The reference channels used for the example discharges in figure 17 were picked to coincide with the location of the QCM maximum amplitude. For plasmas without a QCM, the reference channel was chosen at the same ρ_{pol} as the EDA and QCE discharges, except for the I-mode discharge, where the reference channel was picked as the channel which shows the maximum amplitude of the weakly-coherent mode (WCM). As shown, the phase change behavior is similar between the EDA and QCE phases and unique from the other three phases. Both the L-mode and I-mode show arbitrary values with high uncertainty, even when a fairly coherent mode is present as with the WCM in the I-mode discharge. The standard H-mode shows behavior reminiscent of the QCE and EDA phases, but has high enough uncertainty that it cannot be viewed as significantly different from the zero phase change seen in the other regimes.

To ensure that the behaviors shown in figure 17 are physical and due to the QCM, the frequency bounds used to average over θ_{xy} were changed and the analysis was repeated. Using the same discharge and time interval as in figure 16. Frequency bounds 1–10 kHz, 20–60 kHz, and 150–200 kHz were chosen to be below the QCM (green), coincident with the QCM (blue), and well above the QCM (red) frequency, respectively. As shown in figure 18, only when the frequency average is coincident with the QCM's frequency range does the behavior previously discussed appear in the radial phase evolution, giving confidence to the fact that the QCM is responsible for this behavior.

4. Investigation of instability driver

With the compiled database of many EDA and QCE discharges, studies can be done on what type of instability drives the QCM in each regime. Previous work in AUG has posited that the QCM is driven by some type of ballooning mode instability [20–22]. Work with the THB diagnostic measuring the phase velocity and wavenumbers of the QCM indicate that it is possibly a RBM or KBM [20]. Work using a ball-pen Langmuir probe capable of measuring simultaneous density and potential fluctuations use the measured, anti-correlated density-potential cross-phase to propose it is some electromagnetic mode like the KBM within the confined region of the plasma [21]. This motivates a study of the connections between measurements presented here and drivers KBM instability.

Measured temperature fluctuations can be plotted against common gradient drive terms for these instabilities. The KBM is driven by gradients in the electron and ion temperatures [49], so

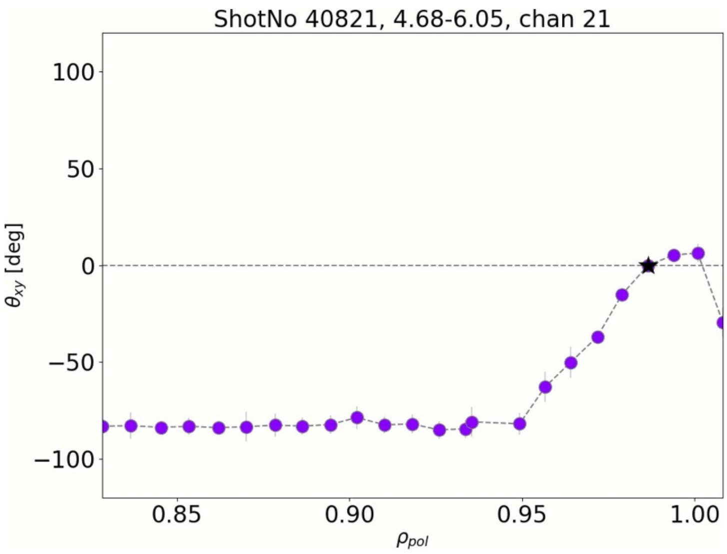

Figure 16. Measured phase difference plotted radially for EDA discharge #40821, using an edge reference channel at $\rho_{\mathrm{pol}} = 0.99$. A constant phase is observed up towards the pedestal top where it quickly increases. A black star is plotted where the reference channel is correlated with itself.

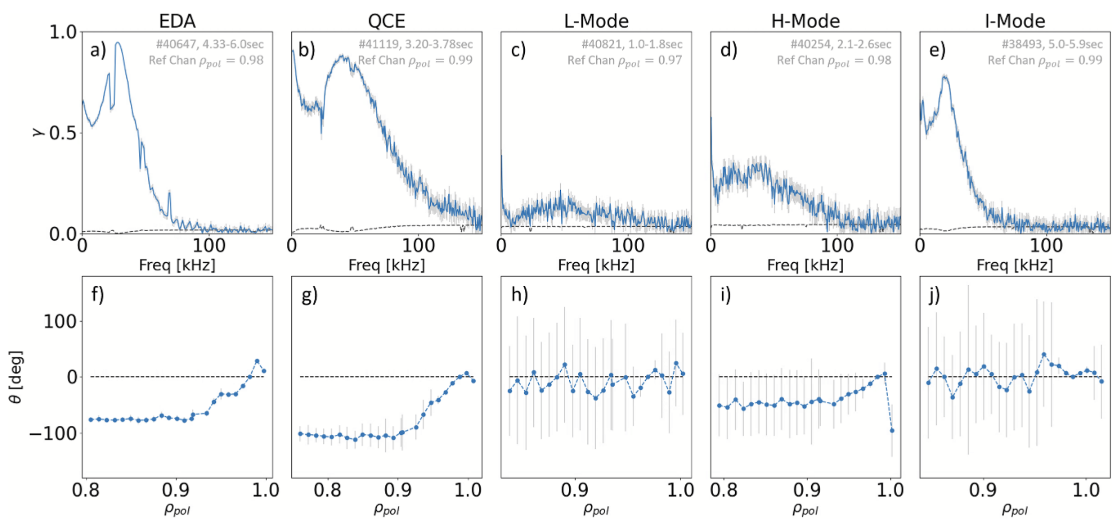

Figure 17. Measured phase changes between CECE channels with respect to the channel located at mode maximum. Subplots (a)–(e) show the γ_c against frequency at the corresponding radial locations as the reference channel used to calculate θ_{xy} in the corresponding subplots of (f)–(j). Shown are plasmas in EDA H-mode in (a) and (f), the QCE regime in (b) and (g), L-mode in (c) and (h), standard (ELMy) H-mode in (d) and (i), and I-mode in (e) and (j). The notch observed around 25 kHz in (a) and (b) is an artifact from filtering out electronic noise.

figure 19 shows the relationship between these drive terms and the measured temperature fluctuations. Because the QCM is located in the edge region of the plasma, only channels measuring in that location were included, specifically $0.96 < \rho_{\mathrm{pol}} < 0.99$ covering the steep gradient region to the pedestal foot. Additionally, measurements of the ion temperature and its gradient require a discharge with NBI heating for good charge-exchange spectroscopy (CXRS) data. As a result the figure 19(b) showing $T_i/\nabla T_i$vs $\delta T_{\mathrm{rad}}/T_{\mathrm{rad}}$ is less populated than figure 19(a) or (c). Plasmas with He as their main ion species could not be included due to a lack of CXRS data.

As shown in figure 19, positive correlations between all three drive terms ($T_{\mathrm{e}}/\nabla T_{\mathrm{e}}$, $T_i/\nabla T_i$, and $p_e/\nabla p_e$) and the measured fluctuations are observed. Though there are fewer points in the comparison, a stronger correlation can be observed from $T_i/\nabla T_i$ in comparison to the other gradient scale lengths. Finally, none of the correlations show a separation between EDA and QCE data points, but those using $p_e/\nabla p_e$ show less scatter than the temperature gradients with the QCE phases generally occurring at higher electron pressure gradient scale lengths than EDA phases. This would seem consistent with the QCM being driven by a KBM instability.

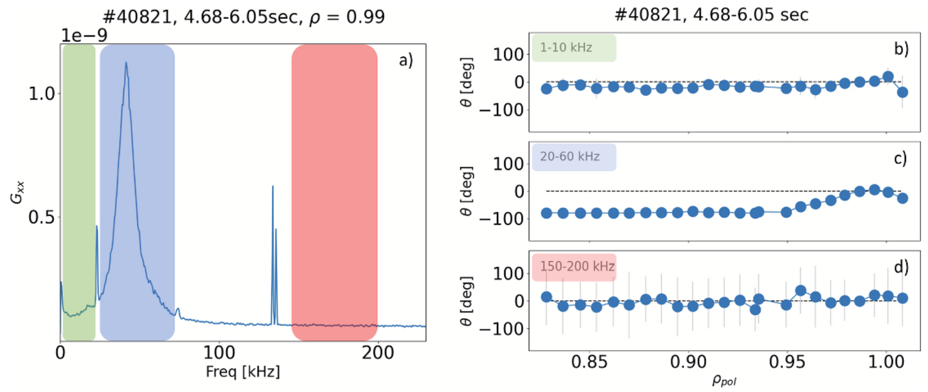

Figure 18. The frequency bounds used to average the phase difference were changed relative to the QCM frequency range. (a) shows the Auto-power of an EDA phase with green, blue, and red boxes highlighting the frequency ranges below, coinciding with, and above the QCM. (b), (c), and (d) show the resulting averaged phase difference for each frequency range, respectively.

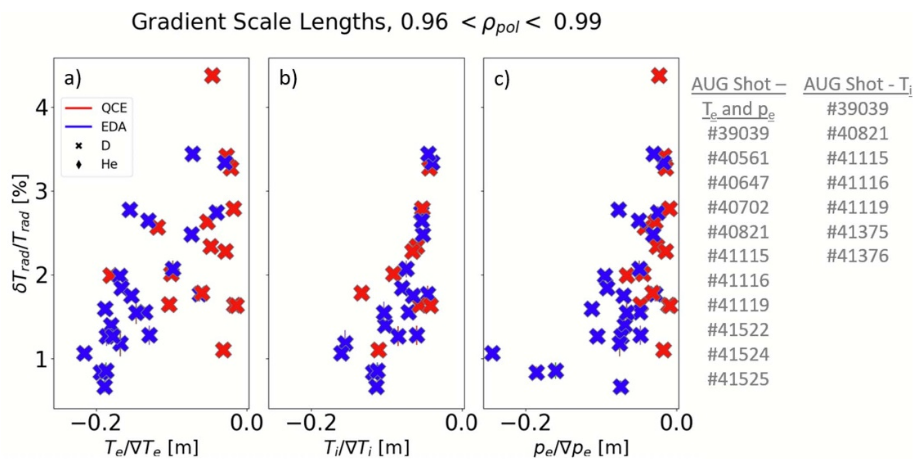

Figure 19. Measured fluctuations, $\delta T_{\text{rad}}/T_{\text{rad}}$, are plotted against KBM drive terms, (a) $T_e/\nabla T_e$, (b) $T_i/\nabla T_i$, and (c) $p_e/\nabla p_e$. Only channels which are between $0.96 < \rho_{\text{pol}} < 0.99$ are included.

Additionally, studies using the collisionality are investigated to understand the importance of collisionality values at the pedestal top against those at the separatrix. It is largely understood that higher edge fueling is necessary to access QCE scenarios, and it is thought that this causes the area at the separatrix to become ballooning unstable, locally [50]. The collisionality, ν^*, is calculated using equation (5).

As expected, higher collisionality values are seen at the separatrix region alongside the highest fluctuation values. However, there is not a clear distinction between EDA and QCE plasmas within the fluctuation-collisionality space shown in figure 20. The electron temperature plays a stronger role in determining the collisionality than the electron density. Even with higher gas puffing resulting in a higher separatrix density in QCE plasmas, the collisionality values for EDA and QCE plasmas occupy similar ranges for discharges within this database.

5. Discussion

Data analyzed from the CECE diagnostic at AUG shows, for the most part, no discernible differences between properties of the QCM in a set of EDA H-mode and QCE plasmas. Radiated temperature fluctuations between each regime are at similar levels of 4%–6%, the spectral widths of the QCM using FWHM fits to the cross-power spectral density are similar between 10-40 kHz, central frequencies of the QCM are between 20-50 kHz, and radial correlation lengths within the steep gradient region fall between 1-2 cm. Additionally, radial evolutions of the phase difference show unique behaviors for QCE and EDA plasmas as compared to other plasma regimes, but not with respect to each other.

When comparing γ_c against G_{xy} or G_{xx} of a given plasma phase, γ_c is always larger in frequency width of the spectra. Due to the normalization of G_{xy} by the corresponding auto-powers, G_{xx} and G_{yy},

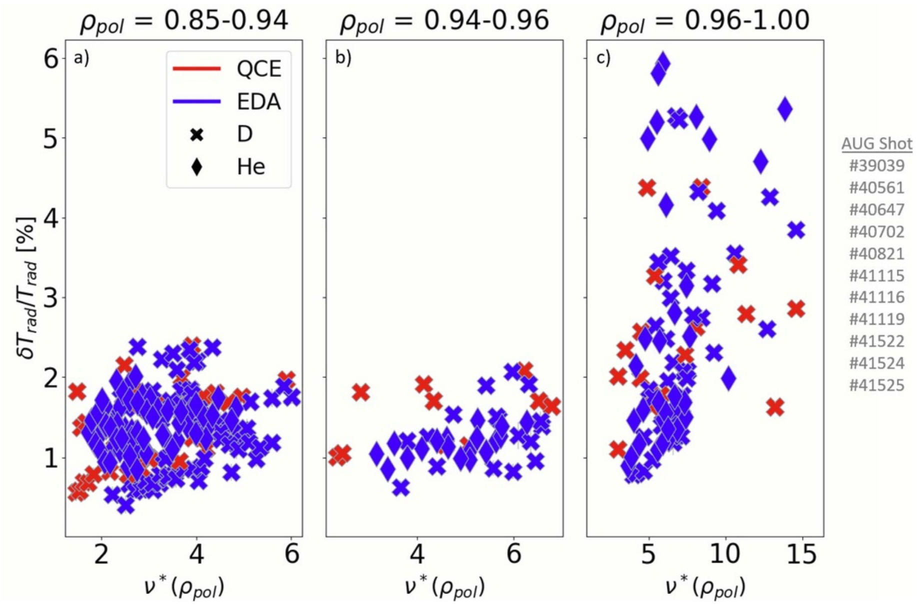

Figure 20. Collisionality was plotted against measured radiated temperature fluctuations. The channel locations were separated into three regions; $0.85 < \rho_{\rm pol} < 0.94$, $0.94 < \rho_{\rm pol} < 0.96$, and $0.96 < \rho_{\rm pol} < 1.0$ to correspond to the outer core region, pedestal top, and steep gradient region.

when calculating $\gamma_{\rm c}$, the lower levels of correlation between the QCM and surrounding broadband turbulence become significant in the coherence spectrum thereby broadening the resulting spectrum. A marked difference between the relationship of these spectral parameters from $\gamma_{\rm c}$ of each phase is observed between EDA and QCE plasmas. When looking at the evolution of the relative bandwidth ($\Delta f/f_{\rm QCM}$) radially in figure 5, it is shown to generally increase for EDA discharges and strongly decrease for QCE. This behavior indicates that the fits performed using $\gamma_{\rm c}$ capture more of the surrounding broadband turbulence than those using G_{xy}. More specifically, this distinction does not necessarily indicate an underlying difference between the QCM in EDA or QCE plasmas, but more that the interaction between the QCM and this broadband turbulence may differ. The exact mechanism for this interaction is unknown and is planned for future study.

Measured radial profiles of $\delta T_{\rm rad}/T_{\rm rad}$ showed no distinction between EDA and QCE plasmas. Both showed similar fluctuation levels at similar radial regions with a peaking close to the separatrix at $4\% - 6\%$. However, figure 7 shows diverging trends between the measured fluctuations when mapped against the central frequency of the fitted QCM, with a negative trend for EDA and positive trend for QCE. This represents a marked difference between EDA and QCE phases within the database. A possible explanation for this difference may be due to the edge $E_{\rm r}$ and the resulting shear it generates.

Many QCE and EDA H-mode discharges at AUG have challenges in getting accurate measurements of $E_{\rm r}$ within the edge. Standard diagnostic techniques for this measurement at AUG are to use CXRS [51] and Doppler back-scatter (DBS) reflectometry [52]. However, many EDA H-modes use purely ECRH heating, eliminating the use of CXRS without NBI heating. As well, accurate measurements of $E_{\rm r}$ using DBS are difficult to get due to the high densities found in these plasmas, requiring extra care for proper localization. Accurate measurements can be obtained with careful discharge design (i.e. by using NBI blips for diagnostics). Yet, the majority of the discharges within this database do not have high enough quality measurements to use in this analysis due to inaccurate localizations, too short integration times (i.e. when using NBI blips), failed digitization, or other, similar reasons. Additionally, because the QCE scenario is a high density plasma and CECE cutoff is avoided by using lower densities, the availability of good $E_{\rm r}$ measurements is further reduced even when using phases with NBI heating. In short, though there exists EDA or QCE discharges with these measurements, the majority of the ones which could be included in this database were not a part of that subset. This necessitates the need for an $E_{\rm r}$ proxy.

Often, for studies in the edge of AUG plasmas with high pedestal collisionalities, the assumption that $E_{\rm r}$ is dominated by the electron diamagnetic component at the location where the electron diamagnetic component is strongest, namely in the ∇p_e well, is made [20, 53]. Thus, $E_{\rm r} \approx -\nabla p_e/en_{\rm e}$ at the location

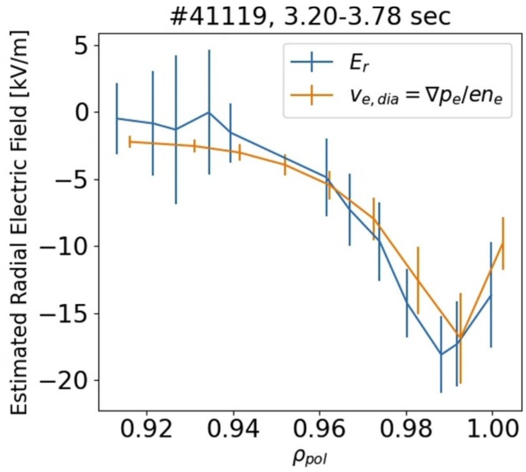

Figure 21. The measured E_{r} from edge CXRS (blue) shows close agreement with the proxy using $\nabla p_e/en_{\mathrm{e}}$ (orange).

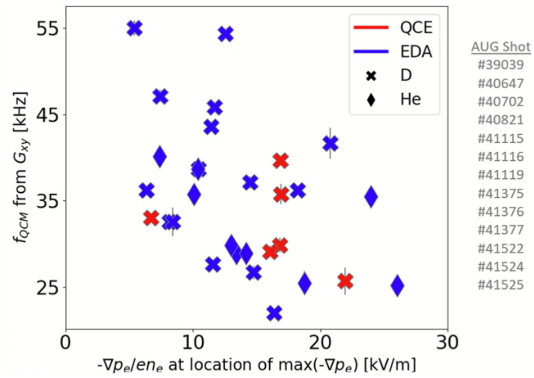

Figure 22. There is a negative correlation between $-\nabla p_e/en_{\mathrm{e}}$ and the center frequency of the QCM. Discharges from the full database are used, and points included in the figure are at radial locations of the minimum of ∇p_e.

of max$(-\nabla p_e)$, where e is the electric charge constant. This assumption is validated using a single discharge from the database with sufficient CXRS data for evaluating E_{r} and it is plotted against $\nabla p_e/en_{\mathrm{e}}$ in figure 21. This use of an E_{r} proxy in this way is commonly done when analyzing EDA H-modes at AUG [13, 20].

With this assumption, insights into the direction of propagation of the mode may be gained by plotting the mode's center frequency against the value of $\nabla p_e/en_{\mathrm{e}}$ as done in figure 22. It is seen that for a stronger $\nabla p_e/en_{\mathrm{e}}$ (plotted with a factor of -1 in figure 22), there is a decrease in the QCM center frequency for both EDA and QCE discharges. This would suggest that the QCM propagates in the ion diamagnetic direction in the plasma frame, but this would only be the case if it is measured to propagate in the ion diamagnetic direction in the lab frame. However, all prior, 2D measurements of the QCM propagation direction have shown it to move in the electron diamagnetic direction in the lab frame [11, 20, 21]. Additionally, power scans at AUG have shown a decrease in the QCM's central frequency with an increasing power level [13], suggesting that the lab velocity decreases with a deepening E_{r} well ($v_{\mathrm{lab}} = v_{E\times B} + v_{\mathrm{phase}}$). This is in agreement with other work that is able to carry out a more extensive analysis in determining the phase velocity of the QCM [21, 54]. The decreasing frequency with increasing input power suggests some characteristic of the QCM (v_{phase}) is changing as E_{r} evolves, but the specific characteristic cannot be determined from this analysis alone.

However, this does not resolve the difference between EDA and QCE phases observed in figure 7 since the same behavior is again observed between EDA and QCE phases in figure 22. Yet, there is a clear effect on the center QCM frequency due to a changing $\nabla p_e/en_{\mathrm{e}}$, and there may be some other process that affects $\nabla p_e/en_{\mathrm{e}}$ differently between QCE and EDA plasmas which gives the resulting difference in figure 7. One such parameter of interest may be the total input power ($P_{\mathrm{tot}} = P_{\mathrm{NBI}} + P_{\mathrm{ECRH}} + P_{\mathrm{ICRH}} + P_{\mathrm{Ohmic}} - \frac{\mathrm{d}W_{\mathrm{MHD}}}{\mathrm{d}t}$). Figure 23 shows there are different trends for $\nabla p_e/en_{\mathrm{e}}$ vs P_{tot} between EDA and QCE

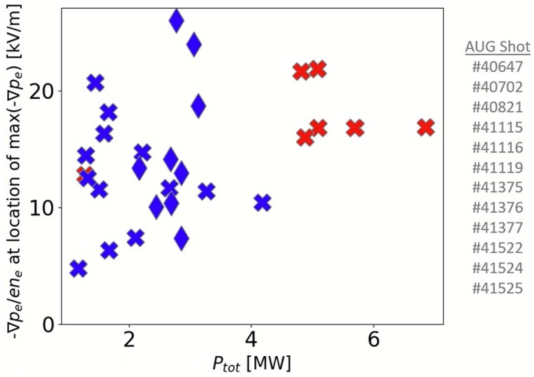

Figure 23. The electron diamagnetic component of E_r is plotted against the total input power of phases within the database. Only points that are located within the ∇p_e well are plotted. A clear positive trend is observed for EDA phases, but QCE displays a heavily scattered trend.

phases within the database. For included EDA phases, a clear positive relationship between P_{tot} and -$\nabla p_e/en_e$ is observed. By association, a higher input power results in a lower center frequency for the QCM in EDA phases. A higher input power would also provide higher temperature fluctuations, coinciding with the behavior seen in figure 7. The story is less conclusive for QCE phases. It remains true that lower center frequencies are associated with higher E_r values (from $E_r \approx -\nabla p_e/en_e$), so it may be that figure 7 shows lower fluctuation values at lower frequencies due to stronger shear effects from the higher E_r. However, it can be seen that the QCE points are enveloped by EDA points—they occupy the same parameter space. It is possible that the database does not contain enough QCE discharges to fully fill out its own parameter space and the limited subset presents a physical trend that may not actually occur. To resolve the issue surrounding the true QCE behavior, an expanded database would be required, but due to diagnostic limitations this was not presently possible with many QCE discharges having to be excluded due to cutoff effects from too high of a density. Resolving this issue would be paramount to properly understanding the radiated temperature fluctuation differences between EDA and QCE plasmas.

Measured values of $\delta T_{rad}/T_{rad}$ are used to calculate displacements, ξ of the plasma's flux surface in the manner done for studying MHD modes. The result showed a broader region over which a maximum ξ is seen for each discharge but at a more inward location than the measured peaks of $\delta T_{rad}/T_{rad}$. It is worth considering the effect that normalizing by the electron temperature gradient has on these measurements and the resulting physical picture. ξ was calculated here in an effort to understand the effects these fluctuations have on the plasma. However, unlike some MHD modes which may be purely driven by ∇T_e, normalizing by this quantity for fluctuations of the QCM disregards the possibility of it being driven by some other term such as a density gradient. It may be worth comparing this method to measured density fluctuations normalized by its own gradient and seeing how the two displacements compare.

Included in the database were EDA discharges which used He as the main ion type so that comparisons against D plasmas could be made. However, throughout the analysis performed, no significant differences were observed. Spectral properties of each plasma (Δf and f_{QCM}), $\delta T_{rad}/T_{rad}$, and L_c all occupied similar parameter spaces. A notable exception to this was the amplitude of a peak observed in ξ (figure 11), though this was mainly due to the overlap between regions of increased $\delta T_{rad}/T_{rad}$ and strong temperature gradients rather than due to a difference in main ion physics. Unfortunately, limited investigations into the role that the main ion has on QCM properties could be obtained due to the strong similarity in experimental design each He discharge had with one another. However, of those included, it is a notable result that properties of the QCM remained unchanged when comparing D and He EDA H-modes. Dedicated experiments which match plasma parameters should be performed to better understand the effects which a plasma's main ion has on the QCM.

The relationship between $\delta T_{rad}/T_{rad}$ and various instability drivers was investigated to understand if the QCM within EDA and QCE plasmas may be driven by differing instabilities. Leading work suggest that the QCM is some type of ballooning mode at the pedestal foot such as a KBM. Comparing various gradient scale lengths such $T_e/\nabla T_e$, $T_i/\nabla T_i$, and $p_e/\nabla p_e$ showed minimal differences between EDA and QCE phases. Interestingly, the strongest correlation was seen between $\delta T_{rad}/T_{rad}$ and the ion temperature gradient scale length indicating that the QCM may be driven by free energy from ∇T_i. Modes driven by

∇T_i include the KBM and ITG which have both been suggested to be the instabilities responsible for the QCM [20].

Yet, the lack of differences observed between the QCM, its properties, and other derived quantities for the EDA and QCE regimes does not necessarily mean these scenarios are identical. The use of the CECE diagnostic limited observations to be within the confined region of the plasma. Valuable measurements could still be made, but the most popular theories distinguishing EDA plasmas from QCE scenarios hinge on differences at the separatrix and SOL regions of the plasma, both regions where measurements from CECE cannot be trusted. It is possible that differences outside of the confined region create distinctions between these two scenarios, but that does not seem to propagate up to the QCM observed in the pedestal.

6. Conclusion

Analysis of CECE data from AUG reveals that the QCM exhibits largely similar characteristics in EDA H-mode and QCE plasmas, including amplitude, spectral width, central frequency, and radial correlation lengths. However, subtle distinctions in how the QCM interacts with broadband turbulence suggest differences in nonlinear coupling or E_r shear dynamics between the regimes.

A significant correlation between QCM amplitude and ion temperature gradient further supports the possibility that the QCM is driven by ∇T_i, consistent with ITG or KBM-type instabilities. Nevertheless, the inability of CECE to probe the separatrix and scrape-off layer limits the conclusions that can be drawn from this dataset alone.

However, any such interactions between the QCM and surrounding broadband turbulence may not just be an important distinction between the QCE and EDA plasma scenarios, but an important mechanism for sustaining the QCE scenario as observed in the pedestal region and hinted at in figure 5. To that end, future efforts are focused towards the use of non-linear gyrokinetic simulations (which have been used to study EDA plasmas in the past [28]) to study differences between distinct QCE and EDA regimes of a single discharge (AUG #41119) to better understand the transition mechanisms that affect the QCM in the pedestal region and provide a validation study with collected CECE measurements.

Future experiments are planned which combine complementary turbulence diagnostics including the THB [55], reflectometer [56], correlation reflectometer-radiometer [43], and probes [57] with CECE to experimentally assess the transport properties of the QCM. Differences in the bandwidth of the QCM between EDA and QCE H-modes which were observed using the THB were not reproduced using the CECE. Experiments which properly overlay these diagnostics where they take measurements at the same location can work towards investigating this discrepancy and determine if it is due to some type of diagnostic effect such as a different sensitivity in k-space. 2D measurements such as from the THB or an ECE imaging system can be used together with measurements of E_r from DBS and CXRS to supplement the results of this work. This would allow for an accurate determination of the direction of propagation of the QCM. This type of fingerprint could be used alongside the other quantities within this work in comparison to those of a synthetic diagnostic from future modeling studies such as with non-linear gyrokinetic simulations. Altogether this would encompass a substantial effort towards accurately identifying the underlying stability of the QCM while building off of the results presented here.

Data availability statement

The data are generally of large size and not usable for others without extensive metadata attached. ASDEX Upgrade is in the process of implementing FAIR principles, but this is partly a European effort in our community and will take a few more years for completion. The data that support the findings of this study are available upon reasonable request from the authors.

Acknowledgments

The authors would like to express their gratitude toward all of those that helped prepare this work through discussions of its results including Joey Kalis, Elisabeth Wolfrum, Jerry Hughes, and Amanda Hubbard.

This work is supported by the US DOE under Award DE-SC0014264. This work has been carried out within the framework of the EUROfusion Consortium, funded by the European Union via the Euratom Research and Training Programme (Grant Agreement No 101052200—EUROfusion). Views and opinions expressed are however those of the author(s) only and do not necessarily reflect those of the European Union or the European Commission. Neither the European Union nor the European Commission can be held responsible for them. This material is based upon work supported by the National Science Foundation Graduate Research Fellowship Program under Grant No 2141064. Any opinions, findings, and conclusions or recommendations expressed in this material are those of the author(s) and do not necessarily reflect the views of the National Science Foundation.

Appendix. List of included discharges in the database

Discharge	Time period [s]	Main ion	Type	P_{NBI} [MW]	P_{ECRH} [MW]	Edge temp [eV]	Edge density [10^{19} m^{-3}]
39 039	2.47–2.78	D	EDA	0	1.791	320	5.0
	2.83–3.19	D	EDA	0	2.573	370	5.1
	3.75–4.75	D	EDA	0	3.240	380	5.4
	5.05–6.90	D	QCE	2.398	0.759	290	5.2
40 561	2.70–4.05	D	EDA	0	1.511	270	5.7
	4.20–4.97	D	EDA	0	2.220	280	6.5
	5.05–5.49	D	EDA	0	2.942	250	6.6
40 647	2.60–3.98	D	EDA	0	1.412	330	4.7
	4.33–6.00	D	EDA	0	1.307	300	4.7
	6.70–7.19	D	EDA	0	1.420	250	4.1
40 702	6.08–6.90	D	EDA	0	1.418	270	4.3
40 821	4.68–6.05	D	EDA	0	1.126	240	5.7
	6.37–7.19	D	EDA	0	1.106	300	5.9
41 115	2.90–4.47	D	QCE	4.901	0	480	4.1
	5.00–5.90	D	QCE	4.861	0	350	5.0
41 116	4.00–5.50	D	QCE	5.015	0	400	5.0
	5.60–6.57	D	QCE	5.004	0	380	5.1
41 119	2.30–2.80	D	QCE	4.895	1.892	440	4.5
	3.20–3.78	D	QCE	2.381	3.218	380	5.6
	3.90–4.48	D	EDA	2.380	1.685	290	5.3
	4.60–5.37	D	EDA	0	3.172	300	5.5
	5.56–5.89	D	EDA	0	2.504	260	5.0
	6.28–6.48	D	EDA	0	1.828	250	4.4
41 375	6.00–7.19	D	EDA	0	0.866	180	4.8
41 376	6.00–7.19	D	EDA	0	1.075	230	4.8
41 377	3.85–5.83	D	QCE	0	1.037	220	5.0
	6.00–7.00	D	EDA	0	1.058	230	5.0
41 522	5.55–5.75	He	EDA	0	2.261	290	5.0
	6.05–6.30	He	EDA	0	2.462	290	5.3
	6.76–6.92	He	EDA	0	2.645	280	5.5
41 524	5.11–5.25	He	EDA	0	2.030	340	4.9
	6.08–6.45	He	EDA	0	2.457	310	5.5
	6.58–6.96	He	EDA	0	2.619	300	5.6
	7.03–7.48	He	EDA	0	2.843	310	5.8
41 525	4.83–6.07	He	EDA	0	2.587	360	4.6
	6.13–6.68	He	EDA	0	2.843	340	4.7

ORCID iDs

J Schellpfeffer 0000-0002-8687-4475
B Vanovac 0000-0003-4031-9318
M Faitsch 0000-0002-9809-7490

L Gil 0000-0002-9970-2154
L Radovanovic 0000-0002-1311-0482
N Bonanomi 0000-0003-4344-3330
R Bielajew 0000-0002-9578-368X
W Burke 0000-0002-9031-7217
G D Conway 0000-0002-3947-4268
C Yoo 0000-0002-1241-3078
A E White 0000-0003-2951-9749

References

[1] Zohm H 1996 Edge localized modes (ELMs) *Plasma Phys. Control. Fusion* **38** 105–28
[2] Kamiya K *et al* 2007 Edge localized modes: recent experimental findings and related issues *Plasma Phys. Control. Fusion* **49** S43–S62
[3] Leonard A W 2014 Edge-localized-modes in tokamaks *Phys. Plasmas* **21** 090501
[4] Eich T, Sieglin B, Thornton A, Faitsch M, Kirk A, Herrmann A and Suttrop W 2017 ELM divertor peak energy fluence scaling to ITER with data from JET, MAST and ASDEX upgrade *Nucl. Mater. Energy* **12** 84–90
[5] Viezzer E 2018 Access and sustainment of naturally ELM-free and small-ELM regimes *Nucl. Fusion* **58** 115002
[6] Maingi R 2014 Enhanced confinement scenarios without large edge localized modes in tokamaks: control, performance and extrapolability issues for ITER *Nucl. Fusion* **54** 114016
[7] Suttrop W *et al* 2011 First observation of edge localized modes mitigation with resonant and nonresonant magnetic perturbations in ASDEX upgrade *Phys. Rev. Lett.* **106** 225004
[8] Viezzer E *et al* 2023 Prospects of core-edge integrated no-ELM and small-ELM scenarios for future fusion devices *Nucl. Mater. Energy* **34** 101308
[9] Takase Y *et al* 1997 Radiofrequency-heated enhanced confinement modes in the Alcator c-mod tokamak *Phys. Plasmas* **4** 1647–53
[10] Mossessian D A, Groebner R J, Moyer R A, Osborne T H, Hughes J W, Greenwald M, Hubbard A and Rhodes T L 2003 Edge dimensionless identity experiment on DIII-d and Alcator *C* -mod *Phys. Plasmas* **10** 689–98
[11] Gil L *et al* (ASDEX and EUROfusion) 2020 Stationary ELM-free H-mode in ASDEX upgrade *Nucl. Fusion* **60** 054003
[12] Paz-Soldan C 2021 Plasma performance and operational space without ELMs in DIII-d *Plasma Phys. Control. Fusion* **63** 083001
[13] Gil L *et al* (the ASDEX Upgrade Team and the EUROfusion Tokamak Exploitation Team) 2025 EDA H-mode in ASDEX upgrade: scans of heating power, fueling and plasma current *Nucl. Fusion* **65** 046002
[14] Greenwald M *et al* 1999 Characterization of enhanced dα high-confinement modes in alcator *C* -mod *Phys. Plasmas* **6** 1943–9
[15] Faitsch M, Eich T, Harrer G, Wolfrum E, Brida D, David P, Griener M and Stroth U 2021 Broadening of the power fall-off length in a high density, high confinement H-mode regime in ASDEX upgrade *Nucl. Mater. Energy* **26** 100890
[16] Harrer G *et al* (The ASDEX Upgrade Team and The EUROfusion MST1 Team) 2022 Quasicontinuous exhaust scenario for a fusion reactor: the renaissance of small edge localized modes *Phys. Rev. Lett.* **129** 165001
[17] Stober J, Maraschek M, Conway G, Gruber O, Herrmann A, Sips A, Treutterer W and Zohm H (ASDEX Upgrade Team) 2001 Type II ELMy h modes on ASDEX upgrade with good confinement at high density *Nucl. Fusion* **41** 1123–34
[18] Faitsch M, Eich T, Harrer G, Wolfrum E, Brida D, David P, Dunne M, Gil L, Labit B and Stroth U 2023 Analysis and expansion of the quasi-continuous exhaust (QCE) regime in ASDEX upgrade *Nucl. Fusion* **63** 076013
[19] Griener M *et al* 2020 Continuous observation of filaments from the confined region to the far scrape-off layer *Nucl. Mater. Energy* **25** 100854
[20] Kalis J *et al* (the ASDEX Upgrade Team and the EUROfusion MST1 Team) 2024 Experimental characterization of the quasi-coherent mode in EDA H-mode and QCE scenarios at ASDEX upgrade *Nucl. Fusion* **64** 016038
[21] Grenfell G *et al* 2024 The multi-faced nature of the quasicoherent mode in EDA H-mode *Nucl. Fusion* **64** 104002
[22] Cathey A *et al* (the JOREK Team, the ASDEX Upgrade Team and the EUROfusion MST1 Team) 2023 Probing non-linear MHD stability of the EDA H-mode in ASDEX upgrade *Nucl. Fusion* **63** 062001
[23] Mazurenko A, Porkolab M, Mossessian D, Snipes J A, Xu X Q and Nevins W M 2002 Experimental and theoretical study of quasicoherent fluctuations in enhanced d α plasmas in the alcator c-mod tokamak *Phys. Rev. Lett.* **89** 225004
[24] Chen B *et al* 2017 Edge turbulence and divertor heat flux width simulations of alcator c-mod discharges using an electromagnetic two-fluid model *Nucl. Fusion* **57** 116025
[25] Macwan T *et al* 2024 ELM-free enhanced d $\boldsymbol{\alpha}$ H-mode with near zero NBI torque injection in DIII-d tokamak *Phys. Plasmas* **31** 122503
[26] Radovanovic L, Dunne M, Wolfrum E, Harrer G, Faitsch M, Fischer R and Aumayr F 2022 Developing a physics understanding of the quasi-continuous exhaust regime: pedestal profile and ballooning stability analysis *Nucl. Fusion* **62** 086004
[27] Cathey A, Hoelzl M, Harrer G, Dunne M G, Huijsmans G T A, Lackner K, Pamela S J P, Wolfrum E and Günter S 2022 MHD simulations of small ELMs at low triangularity in ASDEX upgrade *Plasma Phys. Control. Fusion* **64** 054011
[28] Stimmel K *et al* (the ASDEX Upgrade Team) 2022 Gyrokinetic analysis of an argon-seeded EDA H-mode in ASDEX upgrade *J. Plasma Phys.* **88** 905880315
[29] Creely A J, Freethy S J, Burke W M, Conway G D, Leccacorvi R, Parkin W C, Terry D R and White A E 2018 Correlation electron cyclotron emission diagnostic and improved calculation of turbulent temperature fluctuation levels on ASDEX upgrade *Rev. Sci. Instrum.* **89** 053503
[30] Freethy S J, Görler T, Creely A J, Conway G D, Denk S S, Happel T, Koenen C, Hennequin P and White A E (ASDEX Upgrade Team) 2018 Validation of gyrokinetic simulations with measurements of electron temperature fluctuations and density-temperature phase angles on ASDEX upgrade *Phys. Plasmas* **25** 055903
[31] Cabrera P A M, Rodriguez-Fernandez P, Görler T, Bergmann M, Höfler K, Denk S S, Bielajew R, Conway G D, Yoo C and White A E (ASDEX Upgrade Team) 2023 Isotope effects on energy transport in the core of ASDEX-upgrade tokamak plasmas: turbulence measurements and model validation Phys. Plasmas **30** 082304
[32] Greenwald M *et al* 2014 20 years of research on the alcator c-mod tokamak *Phys. Plasmas* **21** 110501
[33] Vanovac B *et al* (ASDEX Upgrade Team) 2023 Electron temperature fluctuation levels of the quasi-coherent mode across the plasma radius *EPJ Web Conf.* **277** 03003

[34] Bendat J and Piersol A 2012 *Random Data: Analysis and Measurement Procedures* 4th edn, 1st edn (Wiley)
[35] Bielajew R *et al* (the ASDEX Upgrade Team) 2023 Electron temperature fluctuation measurements with correlation electron cyclotron emission in l-mode and i-mode plasmas at ASDEX upgrade *EPJ Web Conf.* **277** 03002
[36] Yoo C, Bielajew R, Conway G D, Cabrera P A M, Rodriguez-Fernandez P, Vanovac B and White A E (the EUROfusion MST1 Team and the ASDEX Upgrade Team) 2023 Database study of turbulent electron temperature fluctuation measurements at ASDEX upgrade *EPJ Web Conf.* **277** 03001
[37] Sauter O, Angioni C and Lin-Liu Y R 1999 Neoclassical conductivity and bootstrap current formulas for general axisymmetric equilibria and arbitrary collisionality regime *Phys. Plasmas* **6** 2834–9
[38] Honda M 2013 Coulomb logarithm formulae for collisions between species with different temperatures *Jpn. J. Appl. Phys.* **52** 108002
[39] Groebner R J and Carlstrom T N 1998 Critical edge parameters for H-mode transition in DIII-d *Plasma Phys. Control. Fusion* **40** 673–7
[40] Rathgeber S K, Fischer R, Fietz S, Hobirk J, Kallenbach A, Meister H, Pütterich T, Ryter F, Tardini G and Wolfrum E (the ASDEX Upgrade Team) 2010 Estimation of profiles of the effective ion charge at ASDEX upgrade with integrated data analysis *Plasma Phys. Control. Fusion* **52** 095008
[41] Denk S S, Fischer R, Maj O, Poli E, Stober J K, Stroth U, Vanovac B, Suttrop W and Willensdorfer M (ASDEX Upgrade Team) 2017 Radiation transport modelling for the interpretation of oblique ECE measurements *EPJ Web Conf.* **147** 02002
[42] Vanovac B *et al* (the ASDEX Upgrade Team and the EUROfusion MST1 Team) 2018 Effects of density gradients and fluctuations at the plasma edge on ECEI measurements at ASDEX upgrade *Plasma Phys. Control. Fusion* **60** 045002
[43] Yoo C, Conway G D, Burke W, Cabrera P A M, Vanovac B, Bielajew R, Cruz-Zabala D J, Silva A and White A E (ASDEX Upgrade Team) 2025 Design of a correlation reflectometer radiometer diagnostic and measurements of the electron density-temperature cross-phase angle in the H-mode pedestal with small edge localized modes at ASDEX upgrade *Rev. Sci. Instrum.* **96** 033504
[44] Fitzpatrick R 1995 Helical temperature perturbations associated with tearing modes in tokamak plasmas *Phys. Plasmas* **2** 825–38
[45] White A 2008 Experimental study of electron temperature fluctuations in the DIII-d tokamak *PhD Thesis* UCLA
[46] Shafer M W, Fonck R J, McKee G R, Holland C, White A E and Schlossberg D J 2012 2d properties of core turbulence on DIII-d and comparison to gyrokinetic simulations *Phys. Plasmas* **19** 032504
[47] Theiler C, Terry J L, Edlund E, Cziegler I, Churchill R M, Hughes J W, LaBombard B and Golfinopoulos T (the Alcator C-Mod Team) 2017 Radial localization of edge modes in Alcator c-mod pedestals using optical diagnostics *Plasma Phys. Control. Fusion* **59** 025016
[48] Watts C 2007 A review of ECE correlation radiometry techniques for detection of core electron temperature fluctuations *Fusion Sci. Technol.* **52** 176–92
[49] Manz P, Boom J E, Wolfrum E, Birkenmeier G, Classen I G J, Luhmann N C and Stroth U (the ASDEX Upgrade Team) 2014 Velocimetry analysis of type-i edge localized mode precursors in ASDEX upgrade *Plasma Phys. Control. Fusion* **56** 035010
[50] Dunne M, Faitsch M, Radovanovic L and Wolfrum E (the ASDEX Upgrade Team) 2024 Quasi-continuous exhaust operational space *Nucl. Fusion* **64** 124003
[51] McDermott R M *et al* (ASDEX Upgrade Team) 2017 Extensions to the charge exchange recombination spectroscopy diagnostic suite at ASDEX upgrade *Rev. Sci. Instrum.* **88** 073508
[52] Lechte C, Conway G D, Görler T and Tröster-Schmid C (the ASDEX Upgrade Team) 2017 X mode Doppler reflectometry k - spectral measurements in ASDEX upgrade: experiments and simulations *Plasma Phys. Control. Fusion* **59** 075006
[53] Viezzer E, Pütterich T, Angioni C, Bergmann A, Dux R, Fable E, McDermott R, Stroth U and Wolfrum E (the ASDEX Upgrade Team) 2014 Evidence for the neoclassical nature of the radial electric field in the edge transport barrier of ASDEX upgrade *Nucl. Fusion* **54** 012003
[54] Kalis J 2024 Characterization of edge modes in different confinement regimes of fusion plasmas *PhD Thesis*
[55] Griener M, Wolfrum E, Cavedon M, Dux R, Rohde V, Sochor M, Muñoz Burgos J M, Schmitz O and Stroth U (ASDEX Upgrade Team) 2018 Helium line ratio spectroscopy for high spatiotemporal resolution plasma edge profile measurements at ASDEX upgrade (invited) *Rev. Sci. Instrum.* **89** 10D102
[56] Cupido L, Graca S, Conway G D, Manso M and Serra F 2006 Frequency hopping millimeter-wave reflectometry in ASDEX upgrade *Rev. Sci. Instrum.* **77** 10E915
[57] Grenfell G *et al* (ASDEX Upgrade Team) 2022 High-heat flux ball-pen probe head in ASDEX-upgrade *Rev. Sci. Instrum.* **93** 023507